Environmental
Science
Processes & Impacts

ROYAL SOCIETY
OF CHEMISTRY

PAPER

View Article Online
View Journal | View Issue

Check for updates

Cite this: *Environ. Sci.: Processes Impacts*, 2022, **24**, 2043

The dependence of soot particle ice nucleation ability on its volatile content†

Kunfeng Gao,[abc] Hans-Christian Koch,[d] Chong-Wen Zhou *[a] and Zamin A. Kanji *[c]

Received 15th April 2022
Accepted 10th August 2022

DOI: 10.1039/d2em00158f

rsc.li/espi

Aviation soot can affect contrail and cirrus cloud formation and impact climate. A product of incomplete combustion, soot particles, are fractal and hydrophobic aggregates comprising carbonaceous spheres with complex physicochemical properties. In the cirrus cloud regime, the surface wettability and pore abundance of soot particles are important determinants for their ice nucleation ability *via* pore condensation and freezing. In the atmosphere, soot particles can undergo various ageing processes which modify their surface chemistry and porosity, thus acting as ice nucleating particles with varying abilities as a function of ageing. In this study, size-selected soot particles were treated by thermal denuding at 573 K in a pure nitrogen (N_2) or synthetic air ($N_2 + O_2$) flow and then exposed to varying relative humidity conditions at a fixed temperature in the range from 218 to 243 K, to investigate the role of volatile content in the ice nucleation ability. Both organic-lean and organic-rich propane (C_3H_8) flame soot particles, as well as two types of commercially available carbon black soot particles with high and low surface wettability, were tested. The size and mass distribution of soot aerosol were monitored during the ice nucleation experiments. Bulk soot samples also prepared in pure N_2 or synthetic air environments at 573 K were characterised by thermogravimetric analysis, Fourier transform infrared spectroscopy and dynamic vapour sorption measurements, to reveal the relation between denuding volatile content, associated soot particle property modifications and the ice nucleation ability. Our study shows that thermal denuding induces a change in soot particle porosity playing a dominant role in regulating its ice nucleation *via* the pore condensation and freezing mechanism. The enrichment in mesopore (2–50 nm) availability may enhance soot ice nucleation. The presence of O_2 in the thermal denuding process may introduce new active sites on soot particles for water interaction and increase soot surface wettability. However, these active sites only facilitate soot ice nucleation when mesopore structures are available. We conclude that a change in volatile content modifies both morphological properties and surface chemistry for soot particles, but porosity change plays the dominant role in regulating soot particle ice nucleation ability.

Environmental significance

The aerosol–cloud-interaction of soot particles is poorly constrained (indirect climate effect). Soot particles with complex and heterogeneous properties are universally found in the troposphere. Soot emission sources co-emit volatile species that can condense or react with the particles thus changing their physical and chemical properties. This process of property modification is termed atmospheric ageing. The complex ageing processes makes it challenging to predict soot particle impacts on ice cloud formation. Here we investigate how the volatile content will influence the physical and chemical properties that are responsible for cloud droplet and ice crystal formation relevant for mixed-phase and cirrus clouds in the troposphere which will have implications for aviation soot induced cloud formation.

1 Introduction

Soot particles are one of the most important non-CO_2 particulate emissions[1] with poorly constrained climate impacts.[2,3] By acting as cloud condensation nuclei (CCN) or ice nucleating particles (INPs), soot particles can form water droplets or nucleate ice crystals, contributing to liquid or ice cloud formation.[4–6] Soot particles emitted by aircraft engines at high altitudes are able to influence aviation contrail evolution and

---

[a] School of Energy and Power Engineering, Beihang University, Beijing, China. E-mail: cwzhou@buaa.edu.cn

[b] Shenyuan Honours College of Beihang University, Beihang University, Beijing, China

[c] Department of Environmental Systems Science, Institute for Atmospheric and Climate Science, ETH Zurich, Zurich 8092, Switzerland. E-mail: zamin.kanji@env.ethz.ch

[d] Bruker Switzerland AG, Fallanden 8117, Switzerland

† Electronic supplementary information (ESI) available. See https://doi.org/10.1039/d2em00158f

further cirrus cloud formation, thereby modifying the cirrus cloud coverage in aviation corridors and modulating regional atmospheric radiative forcing.[7–9] Globally, soot aerosol–cloud interactions can alter both the sign and magnitude of its total annual radiative forcing and the largest uncertainty remains in the cirrus cloud regime.[3,6,10] However, laboratory studies suggest that the ice nucleation (IN) ability of soot particles is poorly constrained, in part because of their complex and heterogeneous physicochemical properties, and also due to varying physiochemical properties during their atmospheric transportation.

There is accumulating evidence from laboratory studies that the pore condensation and freezing (PCF) process is an important pathway for soot IN in the cirrus cloud regime.[11,12] Porosity characteristics and surface wettability are viewed as crucial and decisive properties for soot particle IN *via* PCF.[13–16] PCF favours both mesopore (2 nm < D_p (pore diameter) < 50 nm)[17] structures and a low soot–water contact angle to first induce supercooled water condensation in the pore.[18–20] An ice crystal can form *via* homogeneous freezing of supercooled pore-water when the temperature (T) is lower than homogeneous nucleation temperature (HNT = 235 K) or by immersion freezing at $T > 235$ K if active sites are present within the pore and if the pore size is large enough to host an ice germ at the nucleation temperature.[18] Given that soot particles are a product of incomplete combustion and mainly comprise graphitized primary particles,[21–23] the porosity and surface wettability can be changed by non-carbonized components associated with soot during combustion or by external material coating during atmospheric ageing processes.[24,25] As a result, non-graphitized content changes may interfere with soot particle PCF processes both by changing the pore volume and by influencing the surface wettability.

Laboratory studies suggested that the organic content is of significance to soot particle IN. For example, Möhler *et al.*[26] suggested that the IN ability of propane (C_3H_8) flame soot can be considerably supressed by high level of organic matter (OM) coverage rendering active sites unavailable. This finding is further supported by Crawford *et al.*[27] who showed that soot particles with a 5% OM content by mass are more active INPs compared to those with a 30% OM content. Mahrt *et al.*[11] also suggested that hydrophobic nature of OM in organic-rich C_3H_8 flame soot is responsible for its suppressed IN ability. Zhang *et al.*[28] studied the coating effects of secondary organic aerosol (SOA) on the IN ability of soot particles and noted that SOA coating suppresses soot IN at $T <$ HNT in the cirrus cloud regime by filling in pore structures relevant to PCF. However, Friedman *et al.*[29] found that organic acid coated and size-selected C_3H_8 flame soot particles do not show prominently different IN behaviour for 233 < T < 253 K compared to the uncoated particles. The authors actually observed no IN at $T > 233$ K,[29] which is consistent with a recent study by Kanji *et al.*[30] who reported black carbon particles are not relevant for IN at $T >$ HNT. In contrast to OM addition by coating, Demirdjian *et al.*[31] suggested that the removal of hydrophobic material by heating at 473 K results in enhanced IN for soot particles.

The chemical property of OM on soot particle surface also regulates its IN because the OM content may modify soot particle surface polarity, oxidation level and hydrophilicity. However, conflicting results were reported in the literature. For example, some studies suggested that oxidised soot surfaces promote heterogeneous IN. Gorbunov *et al.*[32] noted that oxidation introduced surface chemical groups enhance soot IN by promoting hydrogen bond formation with water. Kireeva *et al.*[33] and Koehler *et al.*[34] also suggested that oxygen-containing functional groups on soot surfaces may facilitate its IN. Hausler *et al.*[35] reported that surface functionalisation for carbonaceous material increases its hydrophilicity by generating new active sites and thus promoting IN. By contrast, some studies demonstrated that hydrophilicity is not a sufficient predictor for soot IN and low surface oxidation levels facilitate soot IN.[36–40] Whale *et al.*[38] reported that less oxidised carbon nanotubes can nucleate ice more effectively than highly oxidised ones because highly oxidised soot surface with a large polar site density inhibits IN by confining the freedom of water molecules and thus preventing them from rearranging into ice structures. Similarly, Bi *et al.*[39] presented simulation results showing that increased hydrophilicity leads to decreased IN. Most recently, Nichman *et al.*[12] reported that oxidised soot particles freeze homogeneously whereas unoxidised or slightly oxidised soot samples can form ice below homogeneous freezing conditions (HNT and $S_i = 1.4$ (saturation ratio with respect to ice)). The authors deduced that surface oxidation inevitably introduces a change in the soot particle pore structure which is favourable for PCF, though accompanied with surface polarity and hydrophilicity increase.[12] Very likely, soot particle oxidation level or hydrophilicity modification induced by surface OM content change occurs simultaneously with soot particle morphology modifications, thus the combined effects play the role in changing soot IN.[12,35,41] Therefore, determining the role of OM in soot IN requires systematic experimental investigations.

In this study, the dependence of soot particle IN ability on volatile content was investigated under mixed-phase and cirrus cloud conditions. Thermal denuding at 573 K in a pure nitrogen (N_2) or a synthetic air ($N_2 + O_2$) atmosphere was used to change the soot particle volatile content. Then, the IN abilities of size-selected soot particles were observed in a continuous flow diffusion chamber at 218 < T < 243 K. Additionally, systematic measurements characterising the physicochemical properties of soot samples were performed, including soot particle size and mass distribution, the mass of bulk soot volatile content, the chemical composition and functional group changes of soot samples, as well as soot–water interaction activities.

2 Experimental methods

2.1 Instrumentation

In Fig. 1, the experimental schematic is divided into three parts, including sample generation, IN experiments and sample characterisation measurements. A miniature combustion aerosol standard (miniCAST, model 4200, Jing Ltd, Zollikofen, Switzerland) system was used to generate C_3H_8 flame soot under different fuel to air ratios and a dry dispersion setup was utilised

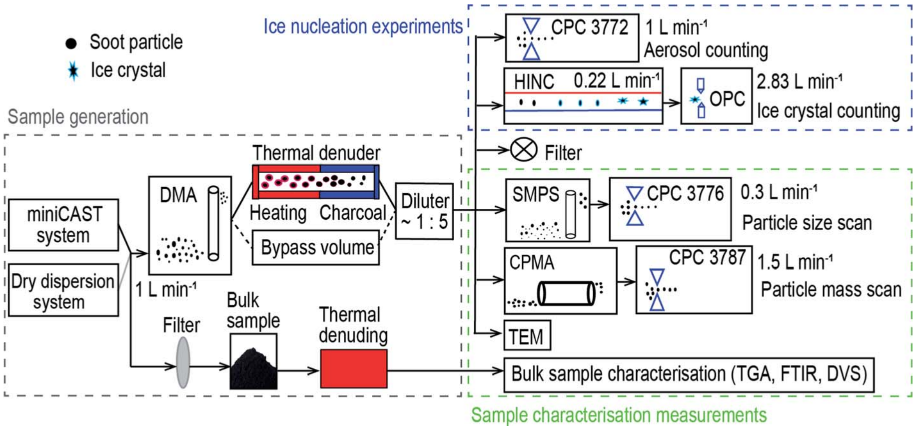

Fig. 1 Schematic of the experimental setup. miniCAST: miniature combustion aerosol standard; DMA: differential mobility analyser; CPC: condensation particle counter; HINC: horizontal ice nucleation chamber; OPC: optical particle counter; SMPS: scanning mobility particle sizer; CPMA: centrifugal particle mass analyser; TEM: transmission electron microscopy; TGA: thermogravimetric analyser; FTIR: Fourier transform infrared spectroscopy; DVS: dynamic vapour sorption.

to disperse two types of carbon black powder. A 1 L min^{-1} aerosol flow was sent through a differential mobility analyser (DMA; classifier 3080, with a 3081 column and a polonium radiation source, TSI Inc.) to select monodisperse soot aerosol particles of 200 or 400 nm. Size-selected aerosol particles were directed to a thermal denuder at 573 K or to a bypass volume before being diluted by a factor of 5. Diluted aerosol sample (5 L min^{-1}) was split into five pathways, including a condensation particle counter (CPC; Model 3772, TSI Inc.) for measuring particle number concentration (1 L min^{-1}), a horizontal ice nucleation chamber (HINC)[42,43] for IN experiments (0.22 L min^{-1}). A high efficiency particulate air capsule (HEPA, PALL Corporation) filter was used for the exhaust flow. A scanning mobility particle sizer (SMPS, classifier 3082, column 3081, CPC 3776 low-flow mode 0.3 L min^{-1}, TSI Inc.) and a centrifugal particle mass analyser (CPMA, Cambustion Ltd, Cambridge, UK) with a 1.5 L min^{-1} flow pulled by a water CPC (model 3787, high-flow mode, TSI Inc.) were used to test particle size and mass distribution, respectively. In addition, 400 nm C_3H_8 flame soot particles were visualised using transmission electron microscopy (TEM) technique. Bulk soot samples were also analysed by thermogravimetric analysis (TGA, Q50, TA Instruments, Eschborn), Fourier transform infrared spectroscopy (FTIR, Tensor 27, Brucker) and dynamic vapour sorption (DVS, Aquadyne DVS-2, 3P Instruments GmbH & Co. KG) measurements.

2.2 Sample generation

Each type of soot sample was denuded at 573 K in either a synthetic air or pure N_2 atmosphere. It is expected that N_2 thermal denuding mainly removes the volatile content from the particle whereas the soot particle surface could oxidise in the presence of O_2 upon thermal denuding in air in addition to volatile content removal. The miniCAST system was operated at fuel/air ratios of 0.95 and 1.03 to generate organic-lean and -rich C_3H_8 flame soot samples, termed mCASTblack and mCASTbrown respectively. Before particle size selection, the combustion exhaust was diluted by a factor of 100 with particle and organic free air (20.9% O_2) through a dilutor (Model VKL100, Palas) and then fed into a 125 L mixing volume to allow particle coagulation and concentration stabilisation. The DMA was used to select 200 or 400 nm soot particles with a sample to sheath flow ratio of 1 : 13 or 1 : 7.3, respectively. Size-selected soot particles were either denuded at 573 K, referred to mCASTblack-air or mCASTbrown-air, or bypassed the thermal denuder before sending to downstream experiments. To denude soot particles under N_2 atmosphere, the Palas dilutor was connected to a pure N_2 (99.99%) source. Generated soot samples were termed mCASTblack-N_2 or mCASTbrown-N_2 hereafter. In addition, commercial carbon black FW200 and Printex90 (Orion Engineered Carbons GmbH, OEC, Frankfurt, Main, Germany) with different graphitization levels were used. Dry carbon black powder was sufficiently stirred for two weeks and then aerosolised by a dry dispersion setup introduced in Gao *et al.*[13] Filtered and organic free air (20.9% O_2) source was used to generate untreated or air denuded carbon black aerosols, termed FW200, PR90, and FW200-air, PR90-air respectively. Pure N_2 source was deployed in the dry dispersion setup to establish an O_2 free thermal denuding atmosphere, by which generated soot samples are termed FW200-N_2 and PR90-N_2. Different soot samples are summarised in Table 1.

For bulk sample characterisation, mCASTblack and mCASTbrown soot were first deposited on filters (PALL, 47 mm, Tissuquartz 2500AQT-UP) by an air pump close to the outlet of the miniCAST and then scraped off. To mimic aerosol particle denuding conditions, soot powders were heated in an oven at 573 K in an air (20.9% O_2) or pure N_2 atmosphere for 6 hours before conducting bulk sample characterisation measurements. For the ease of discussion, oven-heated soot samples are also named using the same suffix as for denuded aerosol particles in the same atmosphere.

2.3 Ice nucleation experiments

Size-selected soot particle IN abilities were measured at a fixed T by running RH (relative humidity) scans in HINC.[42,43] The IN

Table 1 A summary of soot samples used in this study and their characteristic results. The final mass loss at 300 °C is an average value of two individual TGA measurements. The sample functional group changes are with respect to the fresh sample. The particle mobility diameter (D_m) and mass (M_p*) values are derived from the log-normal fitting of particle size and mass distribution curves from SMPS–CPMA measurements, respectively. The hysteresis of the sample DVS isotherms indicates the presence of mesopores in the sample

Type of soot		Thermal denuding atmosphere	Final mass loss at 300 °C	Distinct functional group changes	D_m (nm)		M_p* (fg)		Hysteresis in DVS isotherms
					400 nm	200 nm	400 nm	200 nm	
C_3H_8 soot	mCASTblack	Fresh	1.51%	—	394.5	206.4	7.31	1.78	Yes
	mCASTblack-N_2	N_2	—	C=O, C–O	389.8	206.7	6.82	1.75	—
	mCASTblack-air	Air ($N_2 + O_2$)	0.78%	C=O, C–O	391.4	203.4	7.32	1.78	No
	mCASTbrown	Fresh	11.61%	—	395.4	205.2	6.14	1.14	No
	mCASTbrown-N_2	N_2	—	C=O, C=C, CO–NH, C–O, C–O–C, C–H	307.2	179.7	5.35	0.94	—
	mCASTbrown-air	Air ($N_2 + O_2$)	0.89%	C=O, C=C, CO–NH, C–O, C–O–C, C–H	315.3	178.8	4.46	0.92	Yes
Carbon black	FW200	Fresh	6.82%	—	402.0	202.5	17.07	2.54	Yes
	FW200-N_2	N_2	—	No	397.8	200.5	17.77	2.56	—
	FW200-air	Air ($N_2 + O_2$)	3.25%	No	399.0	198.2	16.90	2.40	Yes
	PR90	Fresh	1.05%	—	405.3	203.0	17.65	2.57	Yes
	PR90-N_2	N_2	—	No	402.4	201.0	17.22	2.57	—
	PR90-air	Air ($N_2 + O_2$)	0.56%	No	400.4	200.9	16.30	2.58	Yes

experiment T range covers cirrus and mixed phase cloud regime from 218 to 243 K and the RH scan at each T with a 2% min^{-1} RH_i (relative humidity with respect to ice) slope starts from ice saturation conditions ($RH_i = 100\%$) and ends at $RH_w = 110\%$ (relative humidity with respect to water). Diffusion dryers were used to reduce the soot aerosol sample RH_w to less than 3%. The concept and principle of HINC operation are elaborated in detail by Lacher *et al.*[43] and Mahrt *et al.*[11] Briefly, a linear T and water vapour pressure profile can be established in the chamber between two ice coated walls at different T (ΔT, $T_{top} > T_{bottom}$). Since the equilibrium vapour pressure is nonlinear as a function of T (Clausius–Clapeyron equation), a RH profile with water sub- and supersaturated conditions can be achieved in HINC. The RH profile can be determined using the parameterisation suggested by Murphy and Koop.[44] Jacketed by a pure N_2 sheath flow, a soot particle aerosol flow (aerosol to sheath flow ratio of 1 : 12) is injected and confined to the centre of the chamber. Hence, RH conditions in the aerosol layer, which is also at the centre of the RH profile, can be determined. Considering an uncertainty of ±0.1 K for T control, the variation of the RH profile across the aerosol layer is calculated to have the largest uncertainty in RH_w of about 5% at the lowest $T = 218$ K and highest $RH_w = 110\%$ condition, and the uncertainty decreases with increasing T and at lower RH conditions. Detailed discussion can be found in Mahrt *et al.*[11] With a fixed aerosol injector position of 25 cm, the particle residence time is approximately equivalent to 10.1–12.3 s for 243 > T > 218 K in the HINC chamber and increases with decreasing T. To evaluate soot particle activated fraction (AF) values, an optical particle counter (OPC) running at different optical size channels, including 1.0, 2.0, 3.0, 4.0 and 5.0 μm, was used to count the number of ice crystals or water droplets ($n_{\text{ice or water droplets}}$) exiting the chamber. The ratio of activated particle number to the total number of soot particles ($n_{\text{soot particles}}$) entering the chamber recorded by the CPC, *i.e.*, the AF, can be calculated according to (eqn. (1)):

$$\mathrm{AF} = n_{\text{ice or water droplets}}/n_{\text{soot particles}} \tag{1}$$

The soot particle AF values can be presented as a function of RH at a fixed T. Soot particles detected by the OPC can be water droplets or ice crystals at T > HNT. Since $S_i > S_w$ (saturation ratio with respect to water), ice crystals grow much larger than water droplets under the same RH and T conditions in HINC. By comparing the AF curves derived from different OPC size channels, the phase of the particle exiting HINC can be discriminated. At the same T as for soot particle IN experiments, we also performed RH scans for 200 nm ammonium nitrate particles (see Fig. S1†) which do not freeze at T > HNT (remain as supercooled liquid droplets) but freeze homogeneously at T < HNT.[43,45] As a reference, we are able to evaluate the particle phase by comparing the AF curves of soot particles to those of ammonium nitrate particles in large OPC channels and at the same T.

2.4 Sample characterisation measurements

2.4.1 TGA. In a N_2 atmosphere, fresh and air-heated (in an oven at 573 K, see Section 2.2) bulk soot samples were analysed by the thermogravimetric analysis (TGA) technique. A precision balance was used to continuously monitor the mass of the soot sample remaining in the furnace with increasing T. The leftover mass percentage can be calculated with respect to original sample mass. The T ramp started from 25 to 300 °C with a constant slope 5 °C min^{-1} and then the T was held constant for 30 minutes at 300 °C to allow sufficient heating and to match aerosol particle denuding experiments. Next, a 10 °C min^{-1} gradient was set to heat the sample to 1000 °C. Two individual runs were performed for each type of soot sample.

2.4.2 FTIR. Both oven-air- and -N_2-heated (at 573 K, see Section 2.2) bulk soot samples, as well as fresh soot samples, were analysed by Fourier transform infrared spectroscopy (FTIR), to investigate thermal denuding induced functional group changes. Bulk soot sample was analysed without any additive agents by ATR (attenuated total reflection) technique using a sampling module equipped with a diamond crystal. The sample was compressed to assure sufficient contact with the crystal surface and measurements were conducted in the range from 400 to 4000 cm^{-1} at a spectral resolution of 2 cm^{-1}. An average of 48 individual scans was reported.

2.4.3 SMPS-CPMA. When assessing the size and mass of denuded soot particles by a SMPS-CPMA system (see Fig. 1), the flow rate and pressure of the whole flow system, as well as the aerosol sample to sheath flow ratio of the upstream DMA for size selection, were kept the same for each type of size-selected soot sample, to achieve the smallest measurement uncertainty. The SMPS was operated with an aerosol sample to sheath flow ratio of 0.3 : 3.0 (0.3 : 1.8) for 200 (400) nm size-selected soot particles, covering a size scanning range 14–594 (19–851) nm, thus including double-charged particle sizes. The CPMA mass scan was performed with a mass resolution better than 3%.

2.4.4 DVS. Samples used for dynamic vapour sorption (DVS) measurements were prepared in the same manner as for TGA. Before measuring soot sample dynamic vapour isotherms, outgassing was performed for bulk soot samples at 573 K under vacuum for 4 hours. At 298 K, the sample mass was recorded and set as a benchmark for the measurements. The adsorption branch of the soot sample isotherm was measured by increasing RH_w conditions from 5 to 90% with a step of 10% then the RH_w was decreased in the same manner down to 5% to measure the desorption branch. Each RH_w condition was maintained for at least 60 min with a RH accuracy ±0.8% and the RH_w condition would only be changed until the mass change (Δm) rate is smaller than 0.001% min^{-1}. As such, a quasi-equilibrium state between the soot sample and water vapour was assumed. Finally, the isotherm was collected in the form of the percentage mass of vapour adsorbed or desorbed as a function of RH_w.

By assessing the soot water vapour isotherm characteristics, water uptake abilities can be qualitatively evaluated.[46,47] The pore-volume based pore size distribution (PSD) of a soot sample as a function of pore radius (r_p) can also be derived.[15,46] The quantitative porosity analysis is based on the Kelvin equation:

$$r_k = -(2\gamma_{sl}\cdot v_s\cdot \cos(\theta))/RT\ \ln(\mathrm{RH_w}/100\%) \qquad (2)$$

where r_k is the Kelvin r_p required for capillary condensation at a certain RH_w below water saturation, γ_{sl} is the interfacial tension of liquid water with respect to a solid, v_s denotes the volume of a water molecule, θ is the soot–water contact angle and the gas constant R equals to 8.314 J mol^{-1} K^{-1}. According to eqn (2), the relationship between RH_w and r_k can be established with assumptions for simplification, including (1) a rigid and cylindrical geometry for pore structures in the soot aggregate, (2) an averaged soot–water contact angle distribution over soot surfaces, (3) the validation of the Kelvin equation over the complete r_p range calculated, (4) homogeneous pore-water-interaction abilities regardless of the pore location. In this study, we modified the mathematical approach for retrieving PSD based on DVS isotherms developed by Wheeler[48] and Shkol'nikov and Sidorova[49] and a high order polynomial fitting method was used to calculate a smoother desorption isotherm function of RH_w. For detailed formulation, we refer the reader to Mahrt *et al.*[15] and Gao *et al.*[16]

2.4.5 TEM. Size-selected mBlack and mBrown particles (400 nm) with and without thermal denuding were also sampled for transmission electron microscopy (TEM, JEOL-1400+, JEOL Ltd, Tokyo, Japan, operated at 120 kV) analysis.

3 Results and discussion

3.1 Ice nucleation dependence on volatile content

3.1.1 Single soot sample ice nucleation results. To evaluate soot particle IN abilities, the onset S_i/S_w value required for a sample to reach an AF value of 0.1% in the 1.0 μm OPC channel is used as a metric. The RH variation that the sample is exposed to in the chamber, is plotted as the uncertainty for each onset S_i. Fig. 2 and 3 summarise the onset S_i results for 400 and 200 nm size-selected fresh soot particles and their denuded counterparts based on individual AF curves in Fig. 9–12 and 13–16, respectively. As indicated by the 1.0 μm water droplet survival line (red dashed line) in Fig. 2 and 3, activated particles could be in liquid or ice phase for $T = 243$ and 238 K. Following the particle phase discrimination method introduced in Section 2.3 and AF curves derived from different OPC channels in ESI S1,† the particle phase is inferred. At 243 K, all 400 and 200 nm soot particles form water droplets as their OPC signals are only present in channels ≤2.0 μm (see ESI S1 Fig. S2–S25),† the same as those of ammonium nitrate particles (see Fig. S1).† At 238 K, all mCASTblack, mCASTbrown, PR90, as well as fresh FW200 particles exiting HINC chamber are water droplets. However, the AF curves of both denuded 400 nm FW200 particles derived from OPC channels ≥4.0 μm at 238 K suggest these particles are in ice phase as their AF values can reach higher than 0.1% when RH_w > 105% for which ammonium nitrate particles (liquid droplets) do not reach an AF of 0.1% at the same RH (see Fig. S1, S9 and S10).† As such, we conclude a fraction of 400 nm FW200-N_2 and FW200-air soot particles can nucleate ice at 238 K.

3.1.1.1 mCASTblack. As shown in Fig. 2a, fresh 400 nm mCASTblack particles require S_w conditions higher than water saturation to form droplets at $T \geq 238$ K, suggesting a hydrophobic surface (consistent with DVS results in Section 3.2.4). Thermal denuding further supresses the water droplet formation ability of mCASTblack as shown by higher onset S_i values for denuded mCASTblack, likely resulting from a decrease in

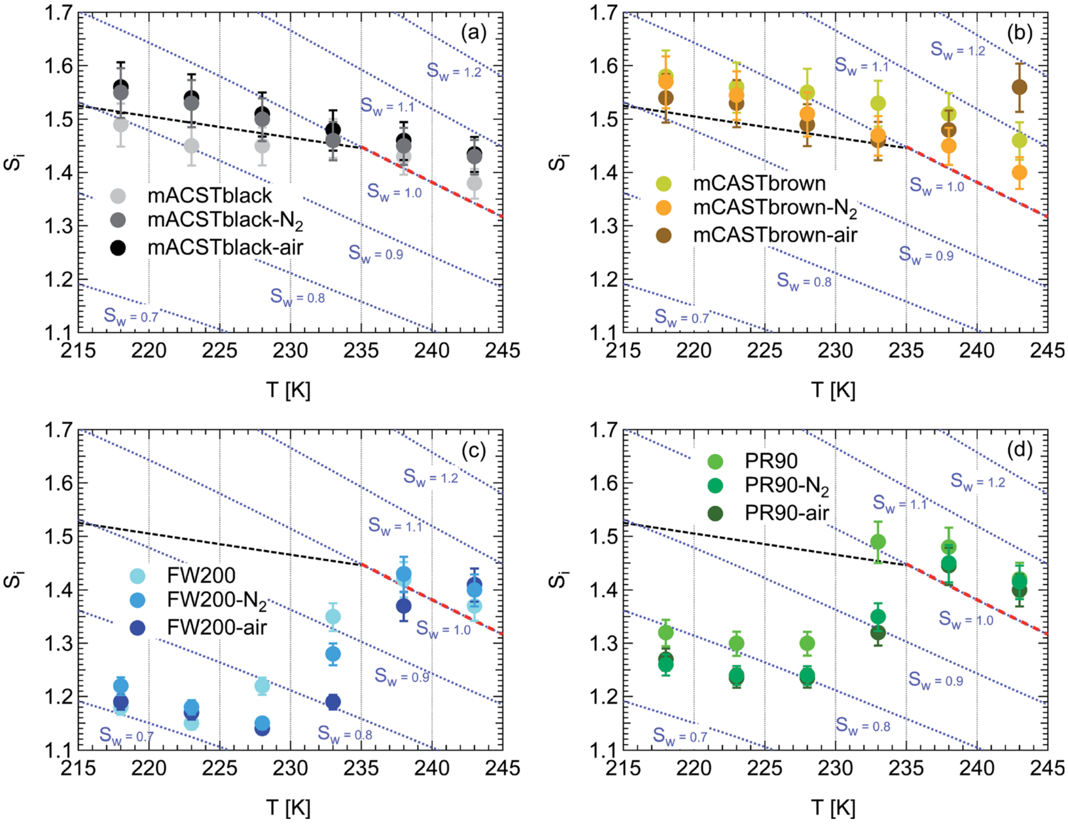

Fig. 2 Onset (at AF = 0.1%) ice saturation ratio (S_i) as a function of T for fresh and denuded 400 nm mCASTblack (a), mCASTbrown (b), FW200 (c) and PR90 (d). AF is reported from the 1.0 μm OPC channel. Black dashed line: homogeneous freezing conditions for solution droplets at T < HNT, according to Koop *et al.*[45] Light blue dotted line: constant water saturation conditions calculated based on Murphy and Koop.[44] Red dashed line: the 1.0 μm size water droplet survival conditions for T > HNT, where the phase of the particle larger than 1.0 μm can be either ice or liquid water. The S_i uncertainty due to the temperature uncertainty (±0.1 K) of the HINC chamber is indicated as error bars. Each data point was derived from the AF curves in Fig. 9–12 presented in the Appendix in which each AF curve is an average of at least two individual RH ramps.

surface water interaction ability because of a decline in pore availability[47,50] caused by thermal denuding. Popovitcheva *et al.*[47] reported that microstructure and porosity play a role in the soot–water interaction of particles emitted by an aero-engine combustor, in addition to hydrophilicity. Thermal denuding at 573 K potentially can fuse non-volatile OM over soot surfaces, resulting in pore blocking. Additionally, the network of non-rigid soot primary particles may be modified due to thermophoretic forces,[51] which decreases the pore openness. For example, Ess *et al.*[52] reported that the nanostructure of C_3H_8 flame soot can be changed significantly after heating in the air up to 773 K. Similarly, both thermal denuding processes inhibit the water droplet activation of 200 nm mCASTblack particles (Fig. 3a), by showing larger onset S_w values above water saturation at the same T compared to the fresh particles.

For $T \leq 233$ K, fresh 400 nm mCASTblack particles freeze at onset S_i values close to the homogeneous freezing threshold ($S_{i,hom}$). After thermal denuding, the onset S_i values of both mCASTblack-N$_2$ and mCASTblack-air particles shift to S_i conditions higher than $S_{i,hom}$. This aligns with the suppressed water droplet activation and suggests that a decrease in pore availability also inhibits soot IN *via* PCF. If the pore is blocked, then liquid water cannot be accommodated for PCF. Whereas if the pore volume becomes smaller, the pore-water will only freeze with a lower homogeneous freezing rate (ω) because it is proportional to the supercooled liquid volume (V) for a fixed T,[45,53] following eqn (3):

$$\omega = J \cdot V \tag{3}$$

where J is the homogeneous freezing rate coefficient as a function of T given as below (eqn. (4)):[54]

$$J = C_{\text{prefac}} \cdot \exp(-\Delta g^{\#}/(k_B T)) \cdot \exp(-\Delta G/k_B T) \tag{4}$$

in which C_{prefac} (1.0×10^{41}, according to Fletcher,[55] Young[56] and Debenedetti[57]) is the preexponential factor, $\Delta g^{\#}$ is the activation energy required for a single molecule to diffuse across the water–ice boundary, ΔG is the energy barrier required for an ice germ formation, k_B is the Boltzmann constant. Hence, both cases explain the absence of PCF for the denuded particles. On the other hand, thermal denuding may increase the pore volume by removing volatile content. However, this is less dominant as the organic-lean mCASTblack does not contain a large amount of volatile OM which can be removed at 573 K (see Section 3.2.1). Despite the speculated potential increase in

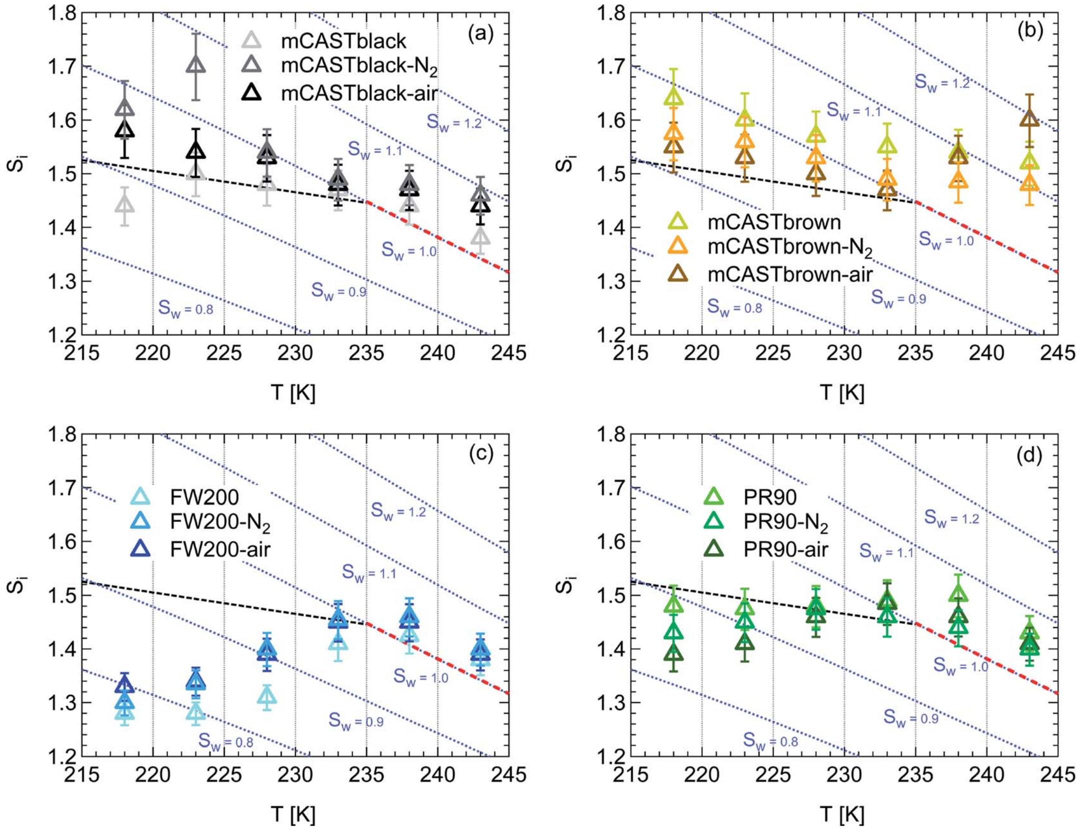

Fig. 3 Onset (at AF = 0.1%) ice saturation ratio (S_i) as a function of T for fresh and denuded 200 nm mCASTblack (a), mCASTbrown (b), FW200 (c) and PR90 (d). AF is reported from the 1.0 μm OPC channel. Black dashed line: homogeneous freezing conditions for solution droplets at T < HNT, according to Koop *et al.*[45] Light blue dotted line: constant water saturation conditions calculated based on Murphy and Koop.[44] Red dashed line: the 1.0 μm size water droplet survival conditions for T > HNT, where the phase of the particle larger than 1.0 μm can be either ice or liquid water. The S_i uncertainty due to the temperature uncertainty (±0.1 K) of the HINC chamber is indicated as error bars. Each data point was derived from the AF curves in Fig. 13–16 presented in the Appendix in which each AF curve is an average of at least two individual RH ramps.

surface oxidation level for mCASTblack-air, simulation and laboratory studies suggest that a higher oxidation level may inhibit soot IN[36–38,40] because a large density of polar functional groups will limit the orientation of water molecules for the ice lattice arrangement.[58] Therefore, mCASTblack-air shows suppressed IN activities. In addition, we note that both thermal denuding processes lead to more pronounced IN suppression for 200 nm particles (Fig. 3a) at the same T compared to those of 400 nm particles (Fig. 2a) as the onset S_i increase induced by thermal denuding with respect to the fresh particle is larger for 200 nm particles, especially for mCASTblack-N$_2$ at $T \leq 223$ K. This probably originates from that thermal denuding leads to a more significant pore volume decrease for smaller 200 nm particles which have a larger effective density (ρ_{eff}) and contain less pore structures scaling to the number of primary particles.

3.1.1.2 *mCASTbrown.* Fresh 400 nm mCASTbrown particles form water droplets at S_w conditions close to 1.1 for T > HNT as shown in Fig. 2b, indicative of hydrophobicity (also consistent with DVS results in Section 3.2.4). Compared to the fresh particles, 400 nm mCASTbrown-N$_2$ particles activate to water droplets at lower S_w but still above water saturation. This is because of volatile removal induced by thermal denuding as the sample contains relatively large amount of hydrophobic volatile OM (see Section 3.2.1). Thus, thermal denuding increases pore openness[51] and exposes active sites,[51,59] both facilitating mCASTbrown-N$_2$ soot–water interaction. In addition, 400 nm mCASTbrown-air particles require an onset S_w condition between those of mCASTbrown and mCASTbrown-N$_2$ to form water droplets at 238 K, but the droplet activation ability is considerably supressed at 243 K as shown by an onset S_w value higher than 1.1. The T dependent water activation depression for mCASTbrown-air particles may coincide with the glass transition T (T_g) change[60,61] for the OM over mCASTbrown-air surfaces. Zhang *et al.*[62] suggested that the T_g of organic aerosol increases with decreased volatility. As such, the T_g of mCASTbrown-air organic material may be increased to above 238 K compared to fresh mCASTbrown particles with a T_g < HNT, because of declined organic volatility caused by thermal denuding in air.[63] Moreover, it is reported that the water vapour uptake by glassy state organics is significantly reduced, hampering the water droplet activation ability.[64–66] Therefore, glassy mCASTbrown-air particles (for 238 < T_g < 243 K) require much higher S_w conditions to form water droplets at 243 K. Whereas mCASTbrown-N$_2$ soot does not show glassy transition because its organic content is different from mCASTbrown-air whose organic content may be oxidised with the presence of

O_2 during air thermal denuding. Also, because light-molecular-weight organics in air denuding may form heavy-molecular-weight organics[51] of low volatility by oxidation, mCASTbrown-air may become more hydrophobic and show supressed water droplet activation compared to mCASTbrown. Besides, original organic-rich mCASTbrown can be thermally decomposed/oxidised at 573 K[52] in the presence of O_2, which makes its graphitization level more like organic-lean mCASTblack-air. For example, Bhandari *et al.*[51] suggested that organic oxidation is already possible for air thermal denuding at $T < 300$ °C. Hence, the mCASTbrown-air with a higher carbonization degree is similar to mCASTblack-air, both of which require S_w condition higher than 1.05 at $T >$ HNT to form water droplets (Fig. 2a and b). Generally, thermal denuding regulates the water droplet activation of 200 nm mCASTbrown particles similarly to 400 nm large particles. N_2 thermal denuding facilitates 200 nm mCASTbrown particles to form water droplets by decreasing the onset S_w values for $T >$ HNT whereas air thermal denuding increases the onset S_w value for 200 nm mCASTbrown particles to activate as droplets especially at 243 K (Fig. 3b).

For $T <$ HNT, fresh 400 nm mCASTbrown particles freeze homogeneously at S_i above the $S_{i,hom}$ whereas both denuded soot particles (mCASTbrown-N_2 and mCASTbrown-air) freeze at lower S_i values than mCASTbrown. The poor IN ability of mCASTbrown may result from a paucity in PCF relevant mesopores and low water uptake abilities because its rich OM content may be hydrophobic and occupy pore structures, both of which impact PCF ability. This aligns with the earlier discussed studies of Möhler *et al.*,[26] Friedman *et al.*[29] and Zhang *et al.*[28] who reported that the IN ability of soot particles is significantly suppressed with increasing OM content or organic coatings. Instead, thermal denuding promotes mCASTbrown-N_2 particle IN due to OM removal. In addition to OM removal, air thermal denuding resulted OM oxidation may increase the OM T_g for mCASTbrown-air particles with decreased OM volatility,[62,63] by which the IN ability of mCASTbrown-air particles may be further promoted. Murray *et al.*[67] and Berkemeier *et al.*[61] suggested that an increase in T_g for soot organics potentially promotes the particle to nucleate ice heterogeneously, which is opposite to its effect for the same sample on water droplet activation. All 200 nm thermal denuded mCASTbrown particles in Fig. 3b present similar IN ability changes following the pattern as those of 400 nm particles presented in Fig. 2b.

3.1.1.3 FW200. The onset S_i values of fresh 400 nm FW200 particles are close to water saturation for $T >$ HNT (Fig. 2c). At 243 K, both denuded FW200 particles require slightly higher S_w conditions than fresh particles to form water droplets, which may result from a decreased soot–water interaction because of the porosity decrease caused by thermophoresis forces.[51] Notably, a small fraction of 400 nm FW200-air soot particles are able to form ice crystals at 238 K as shown by the onset S_i prior to water saturation (see Fig. 2c, 11 and S10b†). Comparing Fig. S9b† (400 nm FW200-N_2) to Fig. S8b† (400 nm FW200), the former may also nucleate ice at 238 K but less than that of FW200-air (Fig. S10b†). Likely, thermal denuding with the presence of O_2 may generate new active sites by oxidation, resulting in more IN active FW200-air particles at 238 K. In Fig. 3c, all 200 nm FW200 particles only form water droplets at $T >$ HNT and both thermal denuding processes do not change the onset S_w values for these particles to activate as droplets (also see AF curves in Fig. 15 and S20–S22†) because of their smaller sizes. Compared to 400 nm particles, 200 nm particles contain a smaller amount of volatiles and have a comparatively lower porosity level[31] as shown a larger ρ_{eff} (see Appendix C). As such, thermal denuding plays a lesser role in regulating the porosity and surface wettability of 200 nm FW200 particles and thus their water droplet activation.

At $T <$ HNT, fresh 400 nm FW200 particles nucleate ice far below $S_{i,hom}$ *via* PCF, which is consistent with the results reported by Mahrt *et al.*[11] who attributed such an active IN ability of FW200 to its strong surface wettability and abundant mesopore structures. Denuded 400 nm FW200 particles nucleate ice more effectively than the fresh counterpart at 233 K as shown by a decrease in onset S_i by 0.07 and 0.16 for FW200-N_2 and FW200-air, respectively (see Fig. 2c and 11). At 233 K, the J coefficient (see eqn. (4)) has a small value as it is highly T dependent,[68,69] thus the ω value, a product of J and liquid volume (see eqn. (3)), can be limited by the small J value close to the HNT.[54] However, if the supercooled liquid volume is large enough, the ω at a T close to the HNT can be compensated.[45,70] By volatile material removal similar to C_3H_8 flame soot, thermal denuding potentially enlarges the FW200 pore volume. Hence, the enlarged pore volume of denuded FW200 particles can promote the PCF processes by increasing ω near the HNT, compared to fresh FW200. Moreover, oxidation may introduce new active sites for FW200-air further promoting its IN by heterogeneous IN.[18] The enhanced IN ability of denuded FW200 particles at 233 K can also be validated by calculations following parameterization reported in the literature. As long as the pore filling occurs at $S_w < 1$, negative pressure induced J promotion can progressively contribute to the homogeneous freezing of supercooled pore-water.[70,71] At 233 K, the parameterization for pressure dependent homogeneous freezing based on the classical nucleation theory (CNT) framework[54] formulated by Marcolli[71] predicts a J value of 1.5×10^{16} m^{-3} s^{-1} at water saturation ($P = 0.1$ MPa), which increases to 4.8×10^{17} m^{-3} s^{-1} at the onset S_w (0.88 in Fig. 11, $P = -13.2$ MPa) for 400 nm FW200-N_2 pore filling and to 5.9×10^{18} m^{-3} s^{-1} at the onset S_w (0.81 in, Fig. 11 $P = -23.2$ MPa) for 400 nm FW200-air pore filling, respectively explaining the observed IN enhancement. Furthermore, the pore size required for capillary condensation at a fixed humidity condition can be calculated according to the Kelvin equation with a soot–water contact angle assumption of 60° for fresh FW200.[19] Considering denuding effect, FW200-N_2 may have a similar contact angle (60°) to fresh FW200 and oxidation may decrease the contact angle for FW200-air (assuming 45°).[46] Then, a cylindrical mesopore with a $r_p = 3.2$ (2.8) nm in 400 nm FW200-N_2 (FW200-air) particles is relevant for pore filling at the onset $S_w = 0.88$ (0.81) and big enough to host an ice germ with a radius 1.14 nm (1.12 nm).[19,20,70] The two r_p values are also within the PSD range of both soot samples (see Section 3.2.4). Following the approach suggested by Koop *et al.*,[45] the freezing time required for the particle in this case to reach the AF = 0.1% is 13.3 (14.9) s for FW200-N_2 (FW200-air), which is close to the HINC particle residence time range (10.1–12.3 s) in this study. Therefore, the above can explain the IN activity of 400 nm FW200-N_2 and FW200-air at 233 K. However, the calculated freezing time for denuded 400 nm FW200 particles at 238 K is larger than the particle residence time in HINC by several orders of magnitude, suggesting supercooled pore-water cannot freeze at 238 K with such a short particle transit time in this study. As such, we must consider that active sites located within the water filled mesopores may nucleate ice through immersion mode freezing.[18] Inside the soot-aggregate pore, surface impurities can serve as potential active sites[72,73] which could have become exposed after air thermal denuding leading to IN *via* immersion mode freezing at 238 K for FW200-air and which are otherwise not present for fresh FW200. Potentially, 400 nm FW200-N_2 particles may also have some active sites exposed by volatile removal and thus nucleate a small fraction of ice crystals at 238 K (see AF curves in OPC channels $\geq$ 4.0 μm in Fig. S9b†).

For $T = 228$ K, the IN enhancement effect brought about by pore enlargement of denuded 400 nm FW200 particles decreases as the T dependent J value increases with decreasing T.[68,69] For $T \leq 223$ K, fresh and denuded 400 nm FW200 particles show comparable IN ability as onset S_i values are within error bars. At a sufficiently low T, the ω is large enough to support the homogeneous freezing of supercooled pore-water regardless of increased porosity due to thermal denuding. As such, 400 nm fresh FW200 particles with abundant PCF relevant mesopores can nucleate ice actively *via* the PCF mechanism and the denuding effect induced active site increase plays a less important role than the case at warmer T (228 to 238 K).

On the contrary, thermal denuding inhibits the IN of 200 nm FW200 particles by increasing the onset S_i values for $T <$ HNT (see Fig. 3c and 15). Different from 400 nm particles, thermal denuding may induce decreased pore volume availability for smaller 200 nm FW200 particles mainly by rearranging the primary particle network and increasing the ρ_{eff} (see Appendix C) and thus leading to a slightly suppressed IN ability.

3.1.1.4 PR90. As presented in Fig. 2d, the onset S_w for fresh 400 nm PR90 particles is about 1.05 at $T >$ HNT and thermal denuding decreases the onset S_w value slightly for PR90-N_2 and PR90-air but the value is still above water saturation. Denuding effects on PR90, including surface modification and morphology restructuring,[51,74] may generate more wettable soot particles which contain more active sites and are more active CCNs. Thermal denuding leads to promoting effects on the water droplet activation of 200 nm PR90 particles (Fig. 3d), similar to the case for 400 nm particles.

Fresh 400 nm PR90 particles freeze homogeneously at 233 K but nucleate ice far below $S_{\text{i,hom}}$ conditions *via* the PCF mechanism for $T \leq 228$ K as containing suitable mesopores to PCF processes.[16] For denuded 400 nm PR90 particles, the onset S_i decreases by more than 0.12 at 233 K, compared to the fresh sample. However, the IN enhancement becomes smaller and the onset S_i values of PR90 soot are within error bars at lower T ($\leq$228 K). Gao *et al.*[16] suggested that the IN of fresh 400 nm PR90 particle *via* PCF is actually ice growth limited at 233 K because its pore volume is too small to support the ice crystal growing out of the pore at such a T close to the HNT[19] at which the J coefficient is also small (following eqn. (4)).[54,68,69] However, if volatile material removal and surface modification decrease the contact angle[51,74] as denuded PR90 already shows enhanced water droplet formation for $T >$ HNT, then the same size mesopores can be filled at lower S_w conditions (<1) or larger mesopores can be filled at the same S_w condition according to the Kelvin equation. Support for the former comes from the fact that the IN of denuded particles is significantly promoted only at 233 K at which a lower S_w for pore filling leads to promoted soot IN *via* PCF by negative pressure induced IN promotion for pore-water.[70] For $T < 233$ K, the J coefficient which is strongly dependent on T, increases with decreasing T (see eqn. (4)),[54] thus the ω at such a low T is sufficient (see eqn. (3)) for the homogeneous freezing of pore-water. As such, the IN promotion brought about by the lower contact angle will not affect denuded 400 nm PR90 at low T (<233 K). On the other hand, larger pore volume filling for denuded PR90 may play a limited role in promoting IN. This is supported by the fact that PR90 only shows a negligible mass loss at the denuding T (573 K, see Section 3.2.1) and presents insignificant changes for mesopore availability (see Section 3.2.4). In addition, the presence of O_2 does not affect the thermal denuding effects on PR90 particle IN, since the onset S_i values of 400 nm PR90-N_2 and PR90-air particles are within error bars at all T tested. This suggests N_2 and air thermal denuding lead to comparable effects on PR90 IN promotion by OM removal or surface oxidation induced soot–water contact angle decrease respectively (see Section 3.2.2). From Fig. 3d and 16, the decrease in onset S_i of 200 nm PR90 particles due to thermal denuding is less pronounced than the case for 400 nm particles at the same T. This is because small size PR90 particles should have less pore volume and less active sites scaling to the surface area.[16]

3.1.2 Ice nucleation comparison between soot samples

3.1.2.1 mCASTblack and mCASTbrown. Thermal denuding shows systematically opposite effects on the IN ability of mCASTblack and mCASTbrown, though the changes are within reported uncertainties (Fig. 2a, b, 3a and b). Thermal denuding supresses the IN ability of mCASTblack particles for $T \leq 233$ K because of decreased pore availability resulting from intra-aggregate change by thermophoresis forces. On the other hand, thermally denuded organic-rich mCASTbrown particles show slightly enhanced IN for $T \leq 233$ K which could be facilitated by increased pore availability induced by more significant OM removal than that of denuded organic-lean mCASTblack. In addition to suggesting that the role of organic content in soot IN is dependent on the combustion conditions, this finding also implies that the organic content itself plays a direct role in regulating soot IN by modifying the intrinsic soot properties such as porosity and surface wettability as will be discussed in section 3.2.

3.1.2.2 FW200 and PR90. There is a significant IN promotion for both denuded 400 nm FW200 and PR90 particles at 228 and 233 K. This finding suggests that soot IN *via* PCF under a T condition close to the HNT is more dependent on the soot particle PSD and surface wettability, compared to lower T conditions. Moreover, the effect of thermal denuding for two types of carbon black samples depends on the particle size but FW200 and PR90 show systematically opposite effects. Thermal denuding suppresses IN for 200 nm FW200 particles, however, it promotes the IN of 200 nm PR90 particles (Fig. 3c and d). This is because thermophoresis forces induced porosity decrease is the overall thermal denuding effect for denuded 200 nm FW200 particles whereas thermal denuding induced surface active site increase and/or soot–water contact angle decrease play the dominant role for denuded 200 nm PR90 particles.

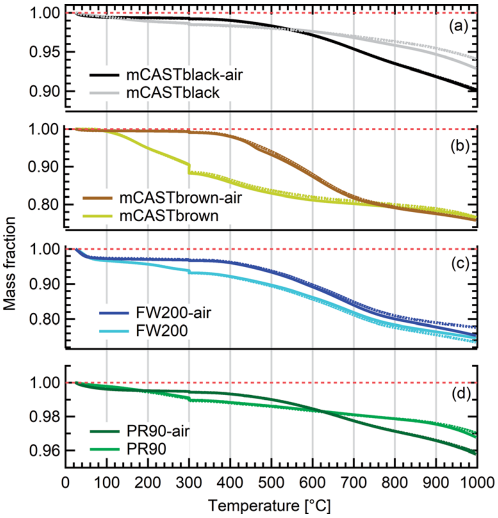

Fig. 4 TGA curves for fresh and oven-air-heated (N_2 + O_2 atmosphere) bulk soot samples. Solid and dotted lines indicate two individual TGA runs. The T was held for 30 minutes at 300 °C. Red dashed line shows the bulk sample mass fraction benchmark, *i.e.*, 100%. Note the different y-axis scales for the samples.

3.2 Volatile content related soot particle property changes

We present soot sample characterisation including bulk soot volatile matter analysis with thermogravimetric analysis (TGA) technique, denuding induced functional group change with Fourier transform infrared spectroscopy (FTIR), the ρ_{eff} of size-selected fresh and denuded soot particles derived from single particle size and mass distribution measurements with SMPS-CPMA (Fig. S26–S33),† as well as soot–water interaction activity with dynamic vapour sorption (DVS) measurement. These results illustrate changes in volatile content and associated changes in soot particle porosity and surface wettability, thus supporting our understanding of soot particle IN abilities. A summary of the characteristic results of soot samples used in this study is provided in Table 1. Exemplary transmission electron microscopy (TEM) images for 400 nm mBlack and mBrown particles with/without thermal denuding are presented in Fig. S34† and used in this section to understand thermal denuding effects on soot particle property and morphology changes. Detailed discussion on TEM images is provided in ESI S3†.

3.2.1 Bulk sample temperature dependent mass loss. In addition to graphitized carbon, soot particles can contain adsorbed water vapour, light-molecular-weight organics and heavy polycyclic aromatic hydrocarbons (PAHs),[22,75,76] which are of different volatilities and thermal lability. In Fig. 4, we plot the thermogravimetric curves of fresh and oven-air-heated bulk soot samples as a function of T. Performed in a N_2 atmosphere, the TGA results for fresh soot samples can be used to deduce the volatile content change of N_2 denuded aerosol samples. Oven-air-heated soot samples at 300 °C prior to TGA measurements were used to represent air denuded aerosol samples.

3.2.1.1 mCASTblack. Fresh mCASTblack exhibits less than 1% mass loss up to T of 100 °C (Fig. 4a), indicating absence of highly volatile OM or large amounts of water vapour.[47,77,78] The sample mass loss up to 300 °C is smaller than 2% (Fig. 4a and Table 1). Heating the sample at $T = 300$ °C for 30 minutes does not lead to a distinct mass decrease (Fig. 4a). According to Ess *et al.*,[52] fuel-lean C_3H_8 flame soot starts to show organic decomposition at $T = 280$ °C. Thus, the results from $T < 300$ °C suggest mCASTblack contains a small proportion of volatile content (<2%). When T increases to 1000 °C, the remaining sample weight fraction is 93%, consistent with the study by Moore *et al.*[79] who reported comparable total organic/volatile content for fuel-lean C_3H_8 flame soot. The mass loss for $T >$ 300 °C is interpreted as loss of heavy-molecular-weight compounds, such as heavy alkanes and PAHs.[52] For mCASTblack-air, a number of points are noteworthy. First, its desorbed mass around 100 °C does not change compared to fresh soot. Second, the mass fraction reduction becomes slightly smaller at $T \leq 300$ °C (Fig. 4a and Table 1), potentially indicative of a decreased volatile OM content after heating with the presence of O_2. In other words, it suggests mCASTblack-air particles for IN experiments may contain less volatile OM than mCASTblack and mCASTblack-N_2 particles. Finally, the total mass loss of mCASTblack-air at 1000 °C is larger than fresh mCASTblack by 3%, suggesting the formation of heavy-molecular-weight organics during air thermal denuding[52,74] and some of those newly formed OM may be decomposed at high T ($300 < T < 1000$ °C).[75] Additionally, such a small mass loss of mCASTblack (Fig. 4a and Table 1) samples at 300 °C cannot be visualised by the corresponding TEM images of 400 nm particles (Fig. S34b and c†) which do not show pronounced morphology changes compared to fresh mCASTblack sample (Fig. S34a†). In general, the low content of hydrophilic volatiles for mCASTblack partly explains its inactive water droplet formation ability and a decrease in volatile content by thermal denuding may lead to droplet activation depression for mCASTblack-N_2 and mCASTblack-air (see Fig. 2a). Moreover, if non-volatile OM can be fused at 300 °C during air thermal denuding they may block pores and supress the IN *via* PCF for mCASTblack-air even further than for mCASTblack-N_2 showing a smaller total OM content, which coincides with the results in Fig. 2a and 3a.

3.2.1.2 mCASTbrown. Both fresh and oven-air-heated mCASTbrown samples show extremely hydrophobic surfaces as the mass loss is negligible (<1%) for $T < 100$ °C, suggesting an absence of adsorbed water and highly volatile OM. Further evidence can be observed from Fig. 17 which shows a flat mass change derivative line close to zero in the same T regime. This explains the poor CCN activation ability of mCASTbrown particles (Fig. 2b and 3b). Upon heating to T = 300 °C, fresh mCASTbrown most likely loses light-molecular-weight OM[80] which can be volatilised below 300 °C.[52,81] The significant mass fraction reduction (>10%) until 300 °C for fresh mCASTbrown (Fig. 4b and Table 1) suggests mCASTbrown-N_2 particles for IN experiments should have less organic coverage thus exposing some pore structures or active sites. However, mCASTbrown-air sample only shows a mass loss less than 1% up to T = 300 °C (Fig. 4b and Table 1), suggesting a substantial volatile OM loss during air thermal denuding at 300 °C (in the oven). The substantial mass losses of mCASTbrown-N_2 and mCASTbrown-air during thermal denuding (at 300 °C) are consistent with the TEM images of these 400 nm particles (Fig. S34e and f†) which show much lacier soot-aggregates caused by OM removal compared to fresh mCASTbrown (Fig. S34d†). It is reported that light-molecular-weight OM reactive to O_2 at high T could be a significant part of the OM content in organic-rich C_3H_8 flame soot particles.[82,83] This part of light-molecular-weight OM in fresh mCASTbrown soot is likely to be oxidised and forms heavy-molecular-weight OM[51] during air thermal denuding at 300 °C (in the oven), supported by an increased mass loss rate for mCASTbrown-air sample for T between 400 and 700 °C (Fig. 4b) due to charring (pyrolysis) during the TGA measurement in a N_2 atmosphere.[51,84,85] Hence, the oxidation of organics may consume some hydrocarbons increasing mCASTbrown-air particle pore availability and reduce the OM volatility influencing the OM phase under low T. As discussed in Section 3.1.1, the decreased OM volatility leads to increased T_g for OM in mCASTbrown-air particles, which promotes particle IN for T < HNT (<T_g)[61,67] whereas inhibits water droplet activation for T > HNT (>T_g),[64–66] compared to mCASTbrown and mCASTbrown-N_2 (Fig. 2b and 3b). Additionally, large total mass losses (24%) for the denuded soot samples at T = 1000 °C suggest that both mCASTbrown and mCASTbrown-air have a lower graphitization degree than mCASTblack. Thus, the non-graphitized OM may decrease the availability of pore structures and active sites for soot particle IN, which explains the less active IN ability of mCASTbrown compared to mCASTblack (see Section 3.1).

3.2.1.3 FW200. Significant mass loss (3%) at T < 100 °C for fresh FW200 soot indicates a large number of hydrophilic active sites on soot surfaces or abundant pore structures for water adsorption. The derivative mass loss curve in Fig. 17 also shows that the mass loss in this T regime mainly occurs at T < 50 °C. This strong water adsorption ability, due to hydrophilic surface sites and/or porous structures,[47,86] also contributes to its active IN ability (see Section 3.1). FW200-air sample shows less than 3% water vapour desorption at T < 50 °C and a flat mass loss curve between 50 and 300 °C (Fig. 4c), suggesting light-molecular-weight OM resistant to 300 °C are completely removed during air thermal denuding. A 7% mass loss for FW200 at 300 °C (Fig. 4c and Table 1) also implies that the N_2 thermal denuding leads to a considerable light-molecular-weight OM removal effect for FW200-N_2. Considering that soluble or hydrophilic material usually has a light-molecular-weight and contributes to water droplet formation, hence, denuded FW200 samples show slightly suppressed CCN activation ability (see Fig. 2c and 3c). In addition, the removal of light-molecular-weight OM may result in active site exposure and pore volume increase, both of which enhance denuded FW200 IN (see Fig. 2c). With increasing T, the mass fraction curves of both FW200 soot samples are almost parallel and decrease similarly to approximately 76%. This may indicate that air thermal denuding does not alter the total OM content of FW200-air and may explain the similar onset S_i results of FW200-air and FW200 for T < 223 K and T > HNT.

3.2.1.4 PR90. PR90 sample is of the highest thermal resistance and shows the smallest mass loss of all samples, suggesting that it is highly carbonized. Both PR90-air and PR90 samples contain a small amount of water vapour (<0.5%), as shown in Fig. 4d for T < 100 °C. Nonetheless, PR90-air desorbs a slightly larger amount of vapour than PR90 when T < 100 °C (Fig. 4d). The water vapour may be adsorbed during sample storage after oven-air-heating. This suggests that PR90-air contains more active sites to adsorb vapour, which also contributes to its more active water droplet formation ability for T > HNT (Fig. 2d and 3d). At T = 300 °C, fresh PR90 shows a 1% mass reduction (Fig. 4d and Table 1), suggesting an OM removal effect of N_2 thermal denuding on PR90-N_2 particles, which may promote the soot–water interaction and IN by exposing active sites, *e.g.*, surface defects and functional groups (see Fig. 2d and 3d). However, PR90-air shows a smaller mass loss when T < 300 °C but shows a larger mass loss than fresh PR90 when T > 600 °C. This suggests that some oxidation reactions may occur during air thermal denuding (in the oven), during which the oxidation at 300 °C consumes some light-molecular-weight OM to generate some heavy-molecular-weight OM that can be decomposed when T > 600 °C (during TGA measurements). Potentially, the oxidation modifies PR90-air particles by introducing new active sites which promote PR90-air water interaction and IN *via* PCF (Fig. 2d and 3d).

In general, TGA measurements demonstrate that soot samples have different proportions of volatile substances (*e.g.*, water vapour and light-molecular-weight OM) by showing varying mass losses for T < 100 °C. The low water affinity of C_3H_8 flame soot (mCASTblack and mCASTbrown) corroborates their poor CCN and IN abilities whereas the wettable surface of FW200 contributes to its active CCN and IN ability. Although PR90 and mCASTblack contain similar amount of volatile content, PR90's higher IN ability (see Section 3.1) may be attributed to its more abundant mesopores (see Section 3.2.4). In addition, comparing soot mass fraction curves for both fresh and air-heated mCASTblack or PR90 samples at T = 1000 °C demonstrates that air thermal denuding may lead to soot sample oxidation and a total increase in OM content of a low volatility.

3.2.2 Functional group change deduced from FTIR spectroscopy. Functional groups may distribute over soot surfaces, like hydroxyls, carbonyls and carboxyls. We use FTIR spectroscopy to identify which functional groups are present in our soot samples.[87,88] The interpretation of FTIR spectra can be challenging because the C–H set of vibration in the hydrocarbon spectra is ubiquitous in organic compounds, appearing at different frequency bands.[89] In addition, particular spectrum bands at a certain wavenumber can appear shifted if affected by other chemicals and matrix factors.[90,91] Given that soot samples contain a complex mixture of compounds, the FTIR spectra are superimposed with spectra from different single chemical bonds. As such, the spectra must be interpreted as a whole system.[89] Though spectra libraries are available, simply interpreting the spectra by looking up soot samples may lead to erroneous interpretation because these libraries are limited in scope to industrial chemicals already investigated systematically but an exclusive soot dataset has not been established yet. Nonetheless, we interpret spectra of thermal denuded soot samples to identify the functional group changes, by using previous soot FTIR spectra available in the literature. In this study, the identification of absorption bands was carried out based on reported results of carbonaceous compound standards[92–94] and practical analysis approach recommended by Coates.[89] Vector normalized absorption spectra are presented in Fig. 5 in which functional groups assigned according to results in the literature are marked. The blue line in Fig. 5 corresponds to the wavenumber 1330 cm^{-1} above which is the characteristic region and below which is the fingerprint region. The spectra will be analysed first by looking up the chemical bond characteristic frequency in the characteristic region. We also use the information in the fingerprint region to identify possible functional groups.

3.2.2.1 *mCASTblack.* The spectra of mCASTblack generally show no distinct peaks and are close to those of graphite reported in the literature,[95,96] suggesting that these soot samples are highly graphitized (see Fig. 5a). The weak telescopic vibration between 3000 and 2800 cm^{-1} indicates the presence of C–H for saturated hydrocarbons[97,98] in both fresh and denuded mCASTblack samples. The difference in the spectra between 2100 and 1600 cm^{-1} implies that thermal denuding changes mCASTblack sample C : O ratio. This is because the small peak appearing at 1725 cm^{-1} is ascribed to sp^2 C=O bonds,[99,100] suggesting that thermal denuding may decrease the sample O : C ratio by removing volatile OM containing C=O bonds. The small peak at 1575 cm^{-1} is assigned to C=C bonds,[93,101,102] implying the presence of a small amount of unsaturated hydrocarbons, such as PAHs. In addition, the bending vibration between 1300 and 900 cm^{-1} in the fingerprint region may suggest C–H belonging to hydrocarbons or C–O belonging to oxidised hydrocarbons.[101,102] If it is ascribed to C–H, it suggests that air thermal denuding increases the saturation level of mCASTblack sample. If it is ascribed to C–O, it implies that air thermal denuding increases C–O bonds (1250 cm^{-1}), which coincides with decreased C=O bonds (1725 cm^{-1}) for mCASTblack-air (Fig. 5a).[101,102] This suggests that air thermal denuding leads to the break of double bonds and the formation of more saturated PAHs because of oxidation.[52,74] These functional group changes are consistent with TGA results in Fig. 4a where mCASTblack-air shows smaller mass losses for $T < 550$ °C but a larger mass losses for $T > 550$ °C because some unsaturated hydrocarbon material is oxidised and becomes more heat-resistant.[74] Most importantly, the newly formed saturated hydrocarbons may not only be hydrophobic but also block mCASTblack pore structures, inhibiting the CCN activation and IN of mCASTblack-air particles.

3.2.2.2 *mCASTbrown.* The fresh mCASTbrown spectra show distinct peaks in Fig. 5b, indicating the presence of various functional groups. There may exist C–H bonds[97,98] as a weak stretch between 3100 and 3000 cm^{-1} represents unsaturated hydrocarbons and the telescopic vibration between 3000 and 2800 cm^{-1} represents saturated hydrocarbons. The crossover at

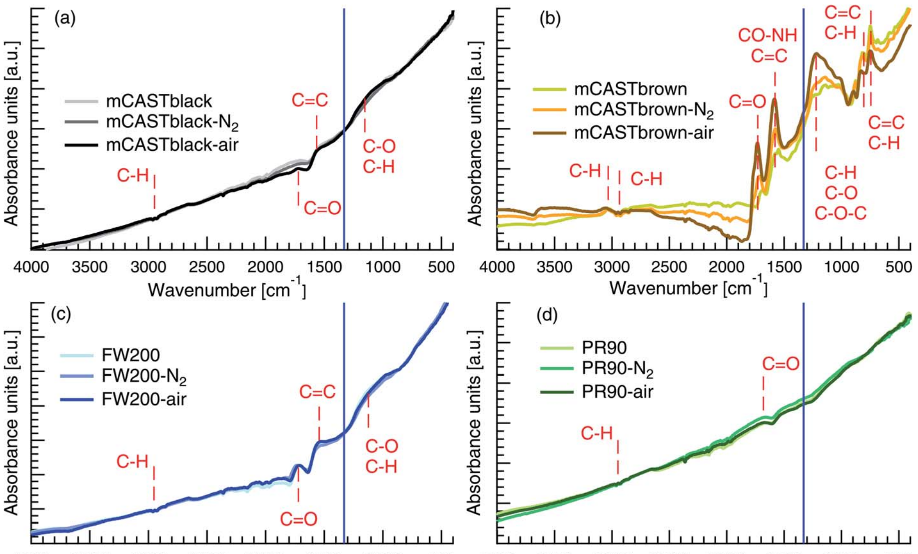

Fig. 5 Vector normalized ATR-AB (Attenuated Total Reflection-Absorption) spectra from FTIR measurements for fresh, oven-air ($N_2 + O_2$)- and -N_2-heated soot. Likely chemical bond assignments are indicated in the individual spectra. The blue line corresponds to the wavenumber 1330 cm^{-1} which separates the characteristic (left) and the fingerprint region (right).

this band range for mCASTbrown sample group potentially suggests the C : H ratio was changed during thermal denuding. The presence of O_2 during thermal denuding magnifies the C : H ratio change trend as mCASTbrown-air specta show the largest slope across the band range. The next spectral feature around 1725 cm^{-1} represents the C═O bond.[99,100] Different from mCASTblack, both thermal denuding conditions increase the C═O bond signal in denuded mCASTbrown. If the C═O bond comes from hydrophilic materials, such as carboxylic acids,[103] then this feature coincides with the opposite IN effects of thermal denuding on mCASTblack (inhibition) and mCASTbrown (enhancement) (see Section 3.1.2). In addition to the C═C bond, the band around 1575 cm^{-1} could be ascribed to amide groups,[104,105] given that the intensity increases after heating in N_2 atmosphere and it increases even further with addition of O_2 during air thermal denuding. Moreover, the noticeable feature in the fingerprint region is that denuded samples show a larger signal in the band range between 1300 and 900 cm^{-1} but present a smaller signal for wavenumber <900 cm^{-1} (see Fig. 5b). Possible bonds in this range can be deduced by linking with the spectral features in the characteristic region, such as C–O–C (1250 cm^{-1}) from epoxy and oxirane rings.[92,106,107] In particular, the single and strong absorption band around 830 and 750 cm^{-1} in Fig. 5b can be ascribed to para- and ortho-aromatic compounds respectively.[89,93,108] Thus, such a band change for wavenumber <1300 cm^{-1} suggests the removal of aromatics[52] (double bonds) and the formation of more saturated hydrocarbons (single bonds) during thermal denuding, especially for mCASTbrown-air. If such an OM content change decreases the OM volatility over mCASTbrown-air particles, it coincides with the T_g shift resulted CCN suppression and IN promotion for mCASTbrown-air particles (see Section 3.1.1.).

3.2.2.3 FW200. In Fig. 5c, fresh FW200 shows modified graphite surface with a telescopic vibration between 3000 and 2800 cm^{-1}, and two small absorption bands at 1725 and 1575 cm^{-1}, as well as a broad band between 850 and 1250 cm^{-1}. These bands can be assigned to C–H bonds from saturated hydrocarbons,[97,98] C═O bonds (carbonyl or carboxyl groups)[107] from heavy PAHs, C═C bonds from aromatic rings[104] or from the carbon skeleton in heavy-molecular-weight organics,[109] and C–H or C–O bonds[101,102,110] from unsaturated hydrocarbons, respectively. The distinct C═O bond generally is linked to the carboxyl group from carboxylic acids[103] which may substantially contribute to the active water interaction and IN ability of FW200 particles (see Section 3.1). Notably, this is different from the case for mCASTblack samples showing a similar spectrum pattern because the much less distinct peaks of mCASTblack samples represent hydrophobic unsaturated hydrocarbons. In addition, the spectra show no significant differences between fresh and denuded FW200 samples. According to the manufacturer, fresh FW200 is highly oxidised carbon black generated by pyrolysis, explaining its resistance to changes in the FTIR spectrum due to thermal denuding. This finding is in line with the TGA results which show parallel mass loss curves for FW200 and FW200-air samples when $T > 300$ °C suggesting similar content of OM for these two samples (Fig. 4c). The similar functionalization level for fresh and denuded FW200 supports their similar CCN activation at 243 K. Since 400 nm denuded samples are more active INPs at $T \geq 228$ and exhibit minor changes in the spectra, it demonstrates that the surface wettability (or soot–water contact angle) plays a secondary role following the porosity change resulted from denuding in the IN of FW200 particles.

3.2.2.4 PR90. In Fig. 5d, fresh PR90 presents a high graphitized surface without distinct bands for functional groups.[95,96] Nonetheless, a weak telescopic vibration between 3000 and 2800 cm^{-1} and a small peak around 1725 cm^{-1} are indicative of the presence of saturated hydrocarbons[97,98] and C═O bonds.[93,101,102] The paucity of functional groups on PR90 samples is supported by the TGA results (Fig. 4d) showing a small amount of total mass losses (3%) at 1000 °C and negligible mass loss at $T < 300$ °C (1%). Thus, such a small OM change by thermal denuding does not lead to detectable functional group changes by the FTIR test. This finding suggests that the enhanced CCN activation and IN for denuded PR90 particles may result from the exposure of particle surface defects but not functional groups as new active sites. The similar FTIR spectra for PR90-N_2 and PR90-air also explains their comparable IN and CCN activation abilities at all T tested (see Section 3.1.1).

In brief, mCASTbrown containing plenty of organic groups exhibits detectable changes induced by thermal denuding in the FTIR spectra. For more graphitized FW200, mCASTblack and PR90, functional group changes from thermal denuding (if any) are not as discernible as in mCASTbrown samples.

3.2.3 Effective density of size-selected soot particle. The SMPS-CPMA measurements were conducted with IN experiments synchronously. Corresponding results of the mobility diameter and mass distribution of soot particles, as well as the evaluation of particle size selection quality are provided in ESI S2.† The single particle mobility diameter and mass results (Table 1) derived from distribution curves are used to calculate the particle ρ_{eff} (see eqn. (C1)) as presented in Fig. 6 (400 nm) and 18 (200 nm). The N_2 thermal denuding may lead to a mass decrease[111] and possibly decrease the mobility diameter by rearranging the primary particle network of the aggregate. Thus, the ρ_{eff} change can be used as a sign to indicate which effect plays the dominant role. The scenario for air thermal

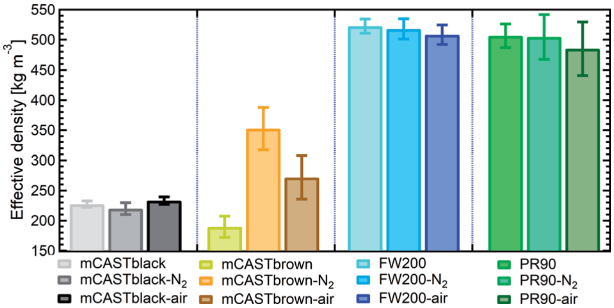

Fig. 6 The effective density (ρ_{eff}) of fresh and denuded 400 nm soot particles. The error bar indicates one standard deviation. Please note the *y*-axis origin.

denuding at 573 K is more complex because oxidation can either reduce the particle mass by burning out combustible material or increase the mass by oxygenation of organics,[51,52] which may change the ρ_{eff} nonmonotonically. Nonetheless, the ρ_{eff} change for size-selected soot particles can be informative about the dominant thermal denuding effect, together with TGA and FTIR results.

3.2.3.1 mCASTblack. Compared to fresh 400 nm mCASTblack, N_2 thermal denuding causes a 3% reduction in ρ_{eff} for mCASTblack-N_2 (Fig. 6), showing that the mass loss plays a more pronounced role than the size decrease (see Fig. S26 and S27† for size and mass changes respectively). This may result in increased porosity,[112] *i.e.*, more pore volume or structures, for mCASTblack-N_2. However, the increased pores are in the micropore[17] range which promote water interaction but are too small for IN *via* PCF for $T <$ HNT (Fig. 2a). A 2.5% ρ_{eff} increase for 400 nm mCASTblack-air particles with respect to fresh mCASTblack results from a small size reduction (smaller than that of mCASTblack-N_2) and an unchanged mass (see Fig. S26 and S27† respectively). It implies that the effect of air thermal denuding on the size and mas of 400 nm mCASTblack-air particles shows a combined effect of OM removal and organic oxidation, by which air thermal denuding decreases the particle mass by OM removal similar to that of mCASTblack-N_2 meanwhile it leads to mass increment and size growth by oxidation, considering the similar denuding (N_2 and air) effect of thermophoresis forces on particle sizes. As such, the oxidation introduced mass increment and size growth compensate more than the mass decrease and size decrease caused by OM removal. Furthermore, new materials produced by oxidation may block pore structures and thus counteract the OM removal effect. This finding coincides with the FTIR results suggesting the formation of more saturated oxygenated hydrocarbons and explains further the IN suppression for mCASTblack-air (Fig. 2a).

3.2.3.2 mCASTbrown. Notably, the ρ_{eff} of 400 nm mCASTbrown-N_2 is doubled compared to mCASTbrown because of a remarkable size decrease (22.3% in Fig. S28b†) but a comparatively small mass decrease (12.9% in Fig. S29a†). In general, this substantial mass reduction removes volatile coatings over soot surfaces and the significant size shrinkage results in more compacted soot–aggregates, both of which increase the pore availability of mCASTbrown-N_2 and thus enhance the particle water droplet formation and IN abilities (Fig. 2b). Compared to mCASTbrown-N_2, the ρ_{eff} of mCASTbrown-air (400 nm) increases only by $\sim$50% with respect to that of mCASTbrown because of a smaller size decrease (20.3% in Fig. S28c†) but a larger mass decrease (27% in Fig. S29a†), still suggesting that thermal denuding leads to significant soot–aggregate compaction and thus promoting soot IN *via* PCF. Such a large mass decrease results from both volatile removal and significant oxidation which oxidises some light-molecular-weight to heavy-molecular-weight OM (see Section 3.2.1 and 3.2.2). These newly formed materials of low volatilities stick to the soot-aggregate, which is supported by the TEM image of 400 nm mCASTbrown-air particle in Fig. S34f† showing OM partially distributed over the soot-aggregate whereas a 400 nm mCASTbrown-N_2 aggregate (Fig. S34e†) shows the more bare primary particles with less OM coverage. Thus, these newly formed OM may support the soot-aggregate structure and prevent size decrease from thermophoresis forces. In addition, these low volatile materials may lead to a higher T_g, thus inhibiting mCASTbrown-air CCN activation for $T > T_g >$ HNT but promoting IN for $T <$ HNT $< T_g$ (see Section 3.1.1). Moreover, the smaller ρ_{eff} of 400 nm mCASTbrown-air also suggests these particles are less densified and have a larger pore volume compared to mCASTbrown-N_2, coinciding with the higher IN ability of 400 nm mCASTbrown-air particles.

3.2.3.3 FW200. The FW200-N_2 only exhibits a slight decrease in ρ_{eff} (<1%) whereas FW200-air shows a larger decrease but still smaller than 3% (Fig. 6). The overall ρ_{eff} decrease mainly results from volatile OM removal which overwhelms the ρ_{eff} increase effect caused by particle mobility diameter decrease (see Fig. S30 and S31† for size and mass changes respectively). The light-molecular-weight OM removal may enlarge soot-aggregate pore structures or uncover some active sites over soot surfaces, such as the exposure of surface defects or functional groups.[73] As a result, both denuded FW200 particles may have increased pore availability and active site density, thus showing promoted IN *via* PCF near the HNT (see Fig. 2c). In addition, the larger ρ_{eff} decrease for FW200-air than FW200-N_2 may be due to a larger mass loss caused by oxidation during air thermal denuding (see Fig. S31a†). The oxidation may consume some volatiles and lead to more significant pore availability increase and/or active site increase, both of which facilitate 400 nm FW200-air particles to nucleate ice more effectively than fresh FW200 particles near the HNT (see Section 3.1.1).

3.2.3.4 PR90. Although containing less total amount of non-graphitized materials, denuded PR90 shows a similar trend in ρ_{eff} change to that of denuded FW200 (Fig. 6). However, the error bars are larger than those of denuded FW200. Nevertheless, the decreased ρ_{eff} for denuded PR90 suggests that the volatile removal represents the major role of thermal denuding for PR90-N_2 and PR90-air particles (see Fig. S32 and S33† for size and mass changes respectively), by which functional groups and surface defects can be exposed and serve as active sites. Consequently, denuded 400 nm PR90 particles show promoted IN and CCN activation (see Fig. 2d). The presence of O_2 during air thermal denuding leads to a larger decrease in ρ_{eff} than N_2 thermal denuding. It suggests the occurrence of oxidation during air thermal denuding. Despite with oxidation, 400 nm PR90-air particles present similar promotion in CCN activation and IN to 400 nm PR90-N_2 particles (see Fig. 2d). Perhaps, this is because original PR90 sample is of high graphitization level and such a weak oxidation (*e.g.*, a small ρ_{eff} change) plays a limited role in modifying the active site density of the particle (Section 3.1.1).

3.2.4 Soot–water interaction activity. For each sample, soot–water interaction abilities are illustrated as DVS isotherms which show the mass percent of water vapour adsorbed (adsorption branch) or desorbed (desorption branch) by per gram of sample with respect to the original sample mass (Δm) as a function of $\mathrm{RH_w}$ (in Fig. 7). In addition to surface adsorption, micropores (at $\mathrm{RH_w} < 40\%$) and mesopores (at $\mathrm{RH_w} > 40\%$) also accommodate water molecules.[47,86] Thus, we present the

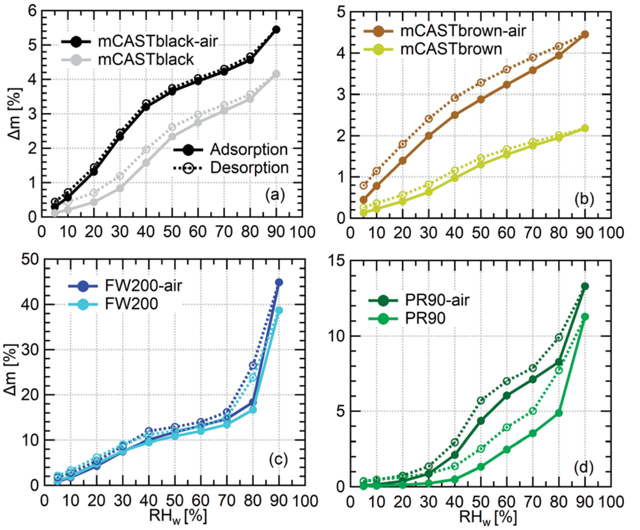

Fig. 7 Dynamic water vapour sorption (DVS) isotherms for fresh and synthetic air ($N_2 + O_2$) oven-heated (300 °C) soot. The solid lines with closed symbols and dashed lines with open symbols indicate adsorption and desorption isotherms, respectively. Each isotherm loop represents for an individual measurement. Note different y-axis scales.

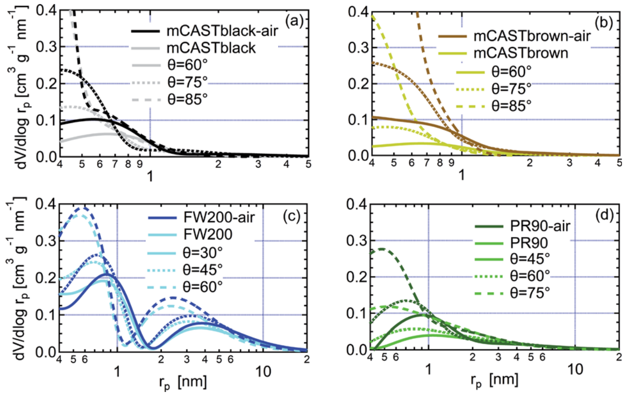

Fig. 8 The pore size distribution (PSD) as a function of pore radius (r_p) for fresh and synthetic air ($N_2 + O_2$) oven-heated soot with different contact angle assumptions, derived from DVS isotherms shown in Fig. 7. (a) mCASTblack, (b) mCASTbrown, (c) FW200, (d) PR90. In each panel, solid line, dotted line and dashed line indicate the PSD results of the same soot sample with different soot–water contact angle assumption values.

volume-based PSD (in Fig. 8) following the methodology introduced in Section 2.4. Considering the heterogeneity of soot surface wettability and thermal denuding introduced alteration, we use three possible contact angle estimates for each sample to calculate the PSD. These estimates are made based on its isotherm characteristics (Fig. 7) and reference values from soot samples of similar isotherms in the literature.[46,113,114] For reference, a perfectly wettable surface has a 0° contact angle.[19,115,116]

3.2.4.1 mCASTblack. Overall, fresh mCASTblack presents a weak water interaction ability and its adsorbed water vapour mass is only 4% at RH$_w$ = 90% (Fig. 7a). Fresh mCASTblack shows a small isotherm slope at low RH$_w$ levels (<40%), suggesting that it may contain a few active sites such as suitable surface defects or hydrophilic functional groups.[59,86] Compared to mCASTblack, mCASTblack-air shows a larger isotherm slope at low RH$_w$ levels (<40%), indicating more abundant active sites for water uptake and a lower contact angle. Notably, enhanced surface wettability of mCASTblack-air does not contribute to its water droplet formation ability for $T \geq 238$ K (see Fig. 2a and 3a) because the removal of water vapour during thermal denuding (see Section 3.2.1) may lead to a water activation delay for mCASTblack-N_2 and -air. Perhaps, non-porous mCASTblack-air particles only activate into water droplets once bulk water condenses onto the hydrophobic surface at $S_w > 1$ whereas fresh mCASTblack particles contain a few pores can accommodate water at $S_w < 1$ and then grow into bulk droplets when $S_w > 1$.[18]

Considering a hydrophobic surface for mCASTblack, large soot-water contact values of 60°, 75° and 85°, are used to calculate the PSD. As shown in Fig. 8a, mCASTblack contains some micropores ($r_p < 1$ nm) and a few mesopores ($1 < r_p < 25$ nm). These pores are also reflected by its isotherms in Fig. 7a. The small offset between its adsorption and desorption branches over the whole RH$_w$ range suggests mCASTblack contains some mesopores leading to isotherm hysteresis. However, a small amount of water can still be preserved in the sample despite substantially decreasing the RH$_w$ condition even down to 5% (see Fig. 7a), suggesting some pore structures are too small to release condensed water, *i.e.*, micropores.[18,86] The small amount of mesopores (Fig. 8a) for mCASTblack coincides with its weak IN ability *via* PCF for $T <$ HNT (see Fig. 2a and 3a). From Fig. 8a, mCASTblack-air contains a few but less mesopores than mCASTblack. The absence of hysteresis between the adsorption and desorption isotherms (Fig. 7a) suggests that mesopores are absent in the sample or it may contain conical or cylindrical mesopores that are closed at the tapered end,[17] which explains its suppressed IN ability compared to fresh mCASTblack for $T <$ HNT (see Fig. 2a and 3a). Note, the approach for PSD analysis only relies on the desorption branch and has a presupposition that there exist pore structures of different sizes (see Section 2.4). Given this approach, we note that the PSD curve of mCASTblack-air in Fig. 8a may be invalid if no pores exist in the sample. Nonetheless, the DVS results qualitatively imply air thermal denuding decreases mCASTblack-air porosity, supporting the discussion about its CCN activation and IN results in Section 3.1.1.

3.2.4.2 mCASTbrown. The mCASTbrown sample is extremely hydrophobic showing an almost linear adsorption isotherm and has the smallest water uptake ability at low RH$_w$ levels (<40%) among all samples (see Fig. 7b). The isotherm slope of mCASTbrown-air is larger than mCASTbrown but its water vapour adsorption only presents a mass increase by 3% at RH$_w$ = 40%. Such a hydrophobic surface explains high S_w conditions (>1.05) are required for the CCN activation of both samples (see Fig. 2b and 3b). Also, the same soot–water contact angle values as estimated for mCASTblack are used for mCASTbrown PSD calculations. Fig. 8b merely shows a mesopore paucity for mCASTbrown, which coincides with the small hysteresis loop of its DVS isotherms (Fig. 7b) and suggests minor pore availability. The mCASTbrown-air has more pores than mCASTbrown as the PSD curve of mCASTbrown-air generally stays above mCASTbrown (Fig. 8b), which results from the removal of volatile content and the exposure of pores by air thermal denuding. The increased pore availability for mCASTbrown-air supports its enhanced IN ability compared to fresh mCASTbrown (see Fig. 2b and 3b) at T < HNT. However, limited PSD enrichment for mCASTbrown-air is not enough to significantly contribute to effective IN *via* PCF because of the initial paucity in pore structures. In addition, the increased pore volume for mCASTbrown-air is mainly attributed to micropores (see Fig. 8b) not relevant for PCF. The enrichment in micropores leads to a stronger water interaction ability for mCASTbrown-air at 298 K by showing a higher isotherm slope (see Fig. 7b) but does not contribute to its CCN activity at 243 K (see Fig. 2b and 3b). This may be because mCASTbrown-air contains some low volatile organics (see Section 3.2.1 and 3.2.2) whose T_g is above the HNT and whose phase transition hampers the CCN activation at 243 K (see Section3.1.1).

3.2.4.3 FW200. According to Thommes *et al.*,[17] the isotherms for FW200 can be classified into Type IVa with a H4 hysteresis loop. This type of isotherm shows a concave curve at low RH_w levels (<40%) and a hysteresis loop at high RH_w conditions (see Fig. 7c), suggesting that FW200 has a hydrophilic surface with plenty of active sites, *i.e.*, a low contact angle, and possesses abundant mesopores. Both its water affinity surface and rich mesopores may contribute to the active IN ability of FW200 particles *via* PCF. In the low RH_w range, water soluble material on the soot surface (see Section 3.2.1) may contribute to its water uptake.[117] Hence, FW200 with a hydrophilic surface can activate as water droplets most readily among all samples (see Fig. 2 and 3). FW200-air shows a similar isotherm slope to fresh FW200 at RH_w < 40% and a larger total water vapour adsorption capacity (Fig. 7c), suggesting that its contact angle is comparable to FW200 and its pore volume is larger than FW200. In addition, the pore volume enlargement in FW200-air may also expose more active sites inside the pore and both effects contribute to the IN promotion of FW200-air at 238 and 233 K (see Section 3.1.1).

Hydrophilic soot with a strong water uptake ability should have a low contact angle between 20–45°.[114] For example, Marcolli *et al.*[19] suggested FW200 soot-water contact angle with a maximum of 60°. Hence, small values (≤60°) are used for FW200 PSD analysis. The PSD results in Fig. 8c demonstrate that there are mesopores of a r_p between 1 and 10 nm dominating the water uptake ability of fresh FW200 at high RH_w levels. Comparing the PSD of both soot samples with the same contact angle assumption (see Fig. 8c), FW200-air PSD curve always stays above FW200, which means it contains more mesopores than FW200. This finding suggests that the enhanced IN for FW200-air is related to the increased mesopore availability (see Section 3.1.1). Moreover, the FW200-air PSD peak is larger and broader than FW200 with all contact angle assumptions (see Fig. 8c), showing that thermal denuding enlarges mesopore volume for FW200-air. The increase in the volume of the same size mesopore also facilitates FW200-air to be more IN active *via* PCF by contributing to the ω of pore-water (see Section 3.1.1).

3.2.4.4 PR90. Fresh PR90 shows an isotherm of Type V with a H3 hysteresis loop,[17,118] showing an isotherm with a convex shape at RH_w < 40% and a broad sorption hysteresis (see Fig. 7d). This suggests it has a relatively low active site density, *i.e.*, a contact angle higher than FW200. Thus, this explains its lower CCN activity compared to FW200 (see Fig. 2 and 3). In addition, because PR90 shows a stronger water uptake ability than C_3H_8 flame soot (Fig. 7d), it is estimated to have a contact angle in the range of 45–75° (<60–85°). Presenting a larger isotherm slope at RH_w < 40%, air thermal denuding lowers PR90-air contact angle and enhances its water affinity. The decreased contact angle also leads to a lower RH_w starting point for PR90-air hysteresis loop, *i.e.*, capillary condensation occurring in smaller mesopores according to the Kelvin equation. The lower the pore filling RH_w is, the stronger the negative pressure induced J promotion of pore-water will be,[70] which supports the IN enhancement of PR90-air particles for T < HNT, especially at 233 K (see Section 3.1.1). Furthermore, assuming a contact angle for PR90-air smaller by 15° than PR90, the PSD results in Fig. 8d suggest that PR90-air contains more micropores (r_p < 1 nm) and small mesopores (1 < r_p < 2 nm) whereas there is no pronounced mesopore change for PR90-air when r_p > 3 nm. Hence, it may be the thermal denuding induced soot–water contact angle decrease and micropore increase that contribute to PR90-air water interaction and CCN activation at T > HNT, and both the decrease in contact angle and the increase in small mesopores that facilitate PR90-air IN *via* PCF at T < HNT (see Fig. 2d and 3d). The contact angle decrease resulted pore filling at low RH conditions may play the first important role in PCF enhancement whereas the mesopore availability change may play a limited role (see Section 3.1.1).

4 Atmospheric implications

This study demonstrates that the IN activity of soot particles depend on their volatile content. Thermal denuding induced property modifications, including intra-aggregate pore volume, chemical functional group and surface oxidation changes, can occur. We note that the results of mCASTblack and mCASTbrown samples containing different OM content can be comparable to aviation soot particles of similar sizes (200 and 400 nm), as these are known to be aviation soot proxies. The mCASTblack and mCASTbrown show similar morphological properties to aviation soot[22,79,119] which may also have varying OM content because of emissions from different engine technologies, thrust levels, and oxidation and/or organic coating during atmospheric transportation. Our findings show that denuding of volatile content by a small mass fraction (≤3% of original particle mass) can lead to enhanced IN *via* PCF for porous soot particles (the case for FW200). We attribute this to an increase in pore volume availability relevant for PCF. On the other hand, it can be deduced that OM oxidation or addition on soot particles may decrease pore availability upon new organics formation and pore network change, thus preventing soot IN *via* PCF (the case for mCASTblack and mCASTbrown). Hence, aircraft soot analogous to mCASTblack and mCASTbrown soot[22,79] may also present suppressed IN ability if OM oxidation or OM coating induced pore availability decrease occurs. Moreover, atmospherically coated soot particles with a small pore availability will not serve as cirrus cloud INPs. Bhandari *et al.*[25] reported that approximately 90% of ambient soot particles sampled from foggy weather conditions are coated, which implies a decreased pore availability and suppressed IN ability with respect to the findings in this study. Freshly emitted and near source soot particles without coatings are thus more relevant to cirrus cloud formation *via* PCF. In addition, our study implies that thermal denuding caused decrease in soot-water contact angle or increase in soot surface active site density may enhance the IN ability of porous soot particles, especially for T close to the HNT (the case for FW200 and PR90). In the atmosphere, porous soot particles can be aged with O_3 producing a more wettable surface,[120–122] after which aged soot particles can contribute to cirrus cloud formation more significantly. Particularly, if porous soot particles are as active as our FW200 sample, then aged porous soot particles with plenty of active sites can even form ice crystals at $T = 238$ K, which is relevant to clouds at lower altitudes. Furthermore, this study has atmospheric implications on the role of physicochemical properties in soot particle water droplet activation at supercooled conditions. Both surface oxidation level and pore availability determine soot-water interaction and droplet activation ability whereas the increased surface oxidation alone may not be the decisive factor. For example, albeit with increased oxidation level, mCASTblack-air shows depressed droplet formation ability as it has decreased pore availability whereas mCASTbrown-N_2 with increased pore availability shows promoted CCN activation for $T >$ HNT. Moreover, the organic phase state for organic-rich soot particles may be important when evaluating the droplet activation and IN ability (the case for mCASTbrown-air). Lastly, it has been shown that mCASTblack can be as active INPs as FW200 merely by compacting the particles through cloud processing, as such ageing by cloud processing after being freshly emitted could lead to a substantial contribution in cirrus cloud INPs.[15]

5 Summary

In this study, different thermal denuding environments (pure N_2 or air) were used to modify four soot samples of various volatile content and porosities, including two C_3H_8 flame soot particles with poor or rich organics (mCASTblack and mCASTbrown), and two porous carbon black particles with high or low surface wettability (FW200 and PR90). Size-selected 200 and 400 nm soot particles with and without thermal denuding were tested for their ice nucleation (IN) ability at fixed temperature (T) between 218 and 243 K, as a function of relative humidity (RH). The particle ρ_{eff} was derived from mobility diameter and mass distribution of size-selected soot samples by conducting SMPS and CPMA scans synchronously with the IN experiments. Bulk soot sample T dependent mass losses, chemical functional group changes and water interaction activities were also measured by TGA, FTIR and DVS techniques, respectively. It is demonstrated that thermal denuding modifies both soot-aggregate porosity and surface water interaction ability depending on the original soot porosity and volatile content, affecting the IN activity of soot particles differently. In general, N_2 thermal denuding may increase soot particle porosity by removing volatile content and meanwhile it may decrease the particle porosity by regulating its primary particle network through thermophoresis forces. Thus, the combined porosity change may be an increase or a decrease which exerts a promotion or impairment effect on the particle pore condensation and freezing (PCF) respectively. Furthermore, volatile matter removal by thermal denuding can expose active sites on soot surfaces for water interaction, contributing to enhanced IN and water droplet activation if sufficient pores are available for the particle. The air thermal denuding regulates soot properties in a more complex manner. In the presence of O_2, surface oxidation may increase the active site density or the product of oxidation may decrease pore openness, which modifies soot particle IN *via* PCF differently. Especially, the air thermal denuding enhances porous soot particle IN near the HNT if the oxidation increases the active site density. Our results imply that the mesopore availability change induced by thermal denuding likely plays a dominant role in regulating soot IN.

Relying on a single predictor to evaluate soot IN activity change may lead to diverse conclusions. Previous studies reported that organic-rich C_3H_8 flame soot particles are poor INPs compared to organic-lean soot produced by the same technique, which potentially suggests that organics inhibit soot IN ability. The thermal denuding results for mCASTbrown soot in this study are consistent with the literature, showing that organics removal promotes soot IN. However, this is opposite to the case for denuded organic-lean mCASTblack soot, which shows supressed IN. Comprehensively, the IN results of denuded mCASTblack and mCASTbrown soot imply that porosity change is the dominant cause for soot particle IN modification but not the organic content change. It is the mesopore availability change associated with removal of organic content that is responsible for regulating soot IN *via* PCF. Other than the organic content, the organic properties, *e.g.*, hydrophilicity, also should be considered in evaluating soot IN abilities. For instance, FW200 soot contains comparable amount of volatile (or organic) content to mCASTbrown soot but it is more CCN and IN active. Therefore, the volatile or organic content alone cannot be used to evaluate soot IN ability. In addition, there is no consensus on the role of oxidation on soot particle IN and contrasting cases are reported in the literature (see Introduction). In the scope of soot PCF, our study suggests that increased soot surface oxidation level (see FTIR in Fig. 5a) associated active site density increase contributes to enhanced soot IN only if the mesopores for PCF are available (see DVS Fig. 8a). Otherwise, oxidised soot surface plays a limited role even if more active sites are exposed. Therefore, we propose that porosity and morphology are primary predictors for soot IN *via* PCF, compared to particle chemistry. To evaluate the single effect of oxidation degree in soot IN, it is promising to only modify the particle surface chemistry and retain its PSD. Finally, soot CCN/IN results at a measured T should be used carefully to infer the results at other T, given that thermal denuding effects on soot CCN/IN showed a *T* dependence (mCASTbrown, FW200 and PR90).

6 Appendix A

6.1 Ice nucleation activity of fresh and denuded 200 nm soot particles

Fig. 9–12 and 13–16 present the AF plots derived from the IN data in 1.0 μm OPC channel for 400 and 200 nm size-selected soot samples as a function of RH_i and RH_w, respectively.

7 Appendix B

7.1 The mass fraction change derivation rates for TGA measurements

Fig. 17 shows the derivative weight fraction change rates for TGA measurements to support the interpretation of the mass loss presented in Fig. 4 in Section 3.2.1. At the beginning of the measurement (<100 °C), rapid mass loss indicates the desorption of water vapour. At 300 °C, the significant mass loss rate is because the *T* was held constant for 30 minutes.

8 Appendix C

8.1 Size-selected soot particle effective density results

The single particle mobility diameter and mass values derived from log–normal fitting to the distribution can be used to calculate the particle effective density (ρ_{eff}) following the expression below:

$$\rho_{\text{eff}} = \left(6M_{\text{p}}^{*}\right) \Big/ \left(\pi \cdot D_{\text{m}}^{\;3}\right) \tag{C1}$$

The M_{p}^{*} is the single particle mass and D_{m} is the single particle mobility diameter. The ρ_{eff} of 400 and 200 nm fresh and denuded particles is presented in Fig. 6 and 18, respectively.

In general, thermal denuding does not result in significant (based on overlapping error bars) ρ_{eff} change for 200 nm mCASTblack, FW200 and PR90 size-selected particles, compared to the fresh particles. It is reported that smaller soot particles have more rigid structure.[123] Hence, thermophoresis forces induced mobility diameter reduction in 200 nm particles is smaller than the case of 400 nm particles, which limits the ρ_{eff} increase. The originally larger ρ_{eff} of 200 nm particles also suggests they have a higher level of compactness and structural stability. This means 200 nm particles present a smaller size change when undergoing the same thermal denuding as larger particles (400 nm). In Fig. 18, the ρ_{eff} change caused by thermal denuding in 200 nm mCASTblack particles shows a similar trend to those of 400 nm mCASTblack particles. The same thermal denuding results in a much smaller ρ_{eff} increase for 200 nm mCASTbrown-N_2 (23%) and mCASTbrown-air (22%) particles (Fig. 18), compared to 400 nm particles (86% and 43% in Fig. 6, respectively). Both thermal denuding conditions lead to an increase in the ρ_{eff} of 200 nm FW200-N_2 and FW200-air

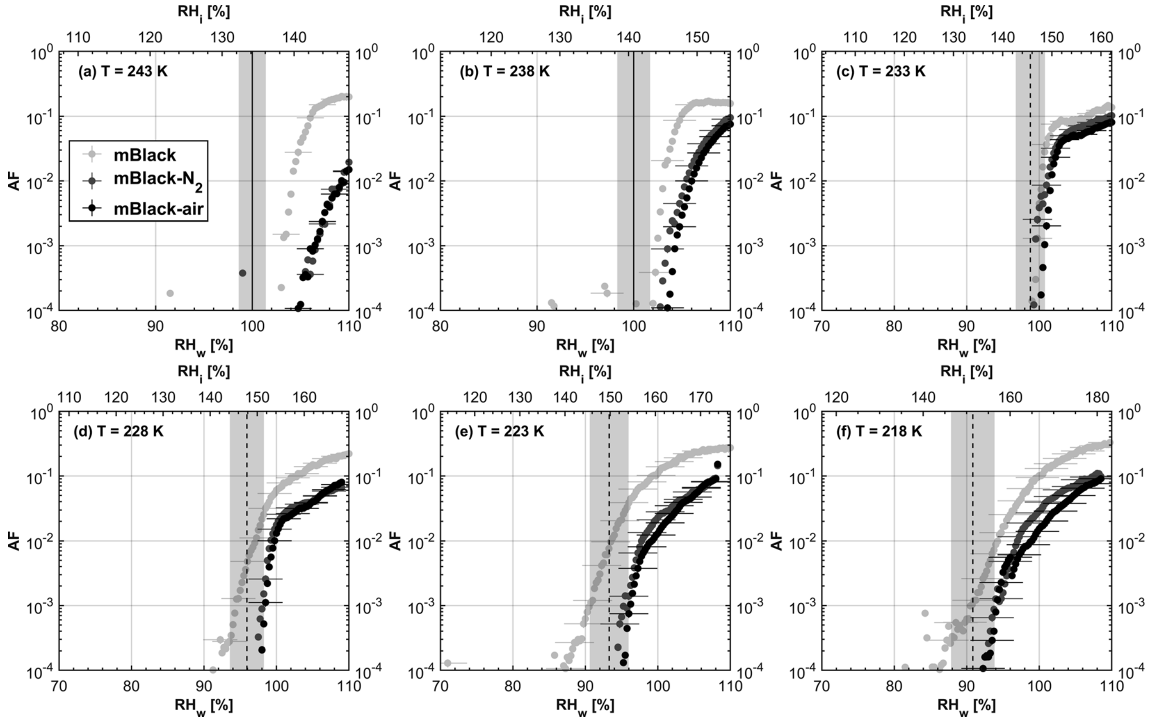

Fig. 9 AF curves as a function of RH (relative humidity) with respect to water (RH_w) and ice (RH_i) for fresh and denuded 400 nm mCASTblack soot particles corresponding to 1.0 μm OPC channel. Black solid line represents water saturation conditions according to Murphy and Koop,[44] and dashed lines indicate expected RH values for homogeneous freezing at *T* < HNT,[45] respectively. The grey shading areas show the possible RH uncertainty calculated for water saturation and homogeneous freezing conditions.

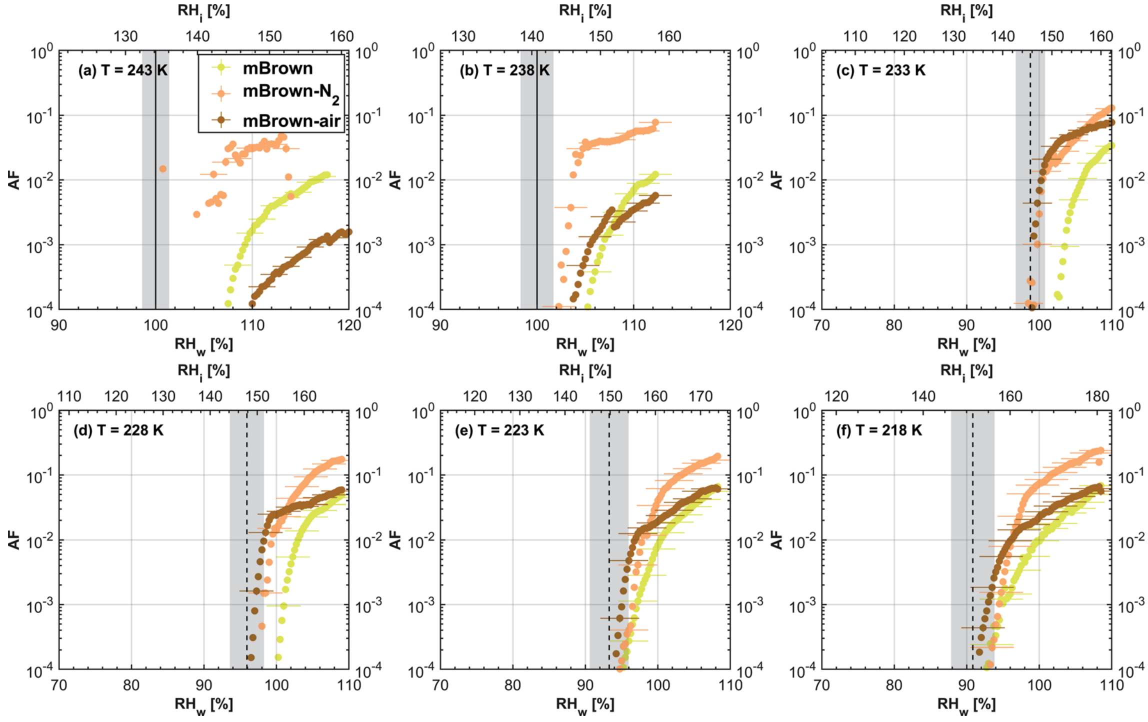

Fig. 10 The same as Fig. 9 but for fresh and denuded 400 nm mCASTbrown soot particles.

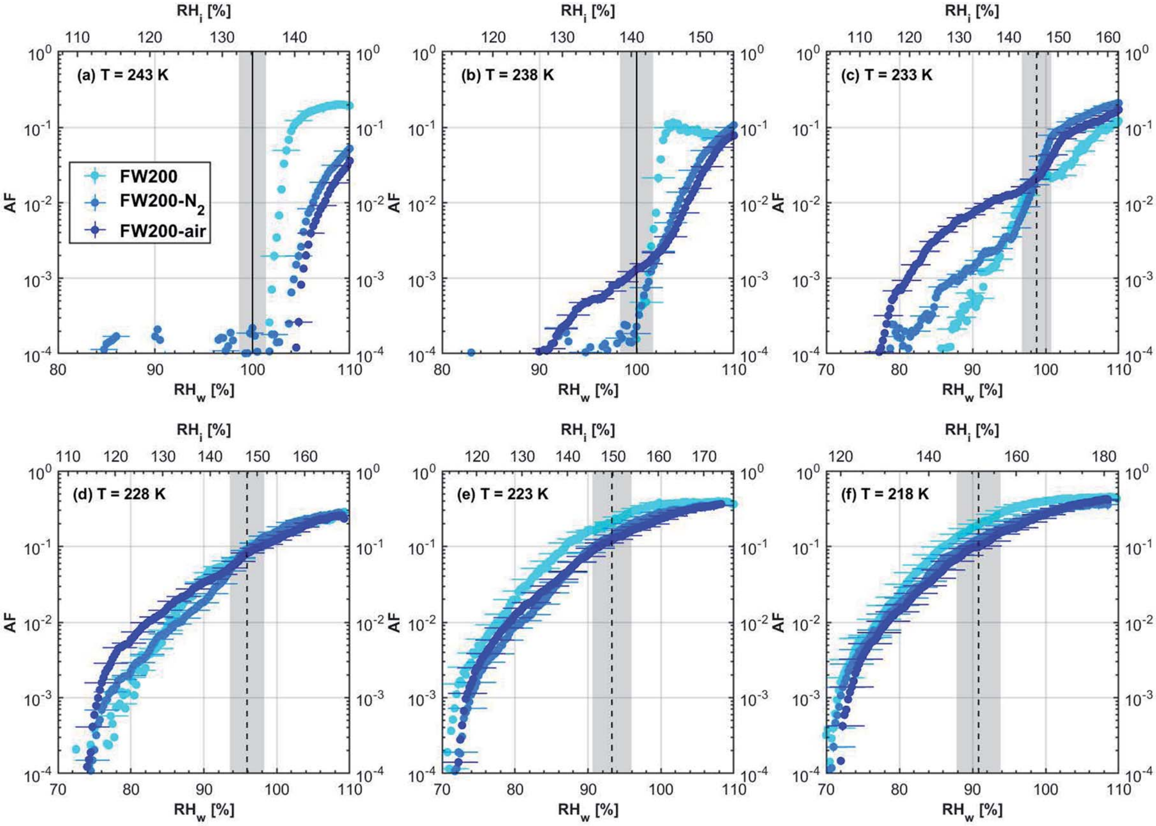

Fig. 11 The same as Fig. 9 but for fresh and denuded 400 nm FW200 soot particles.

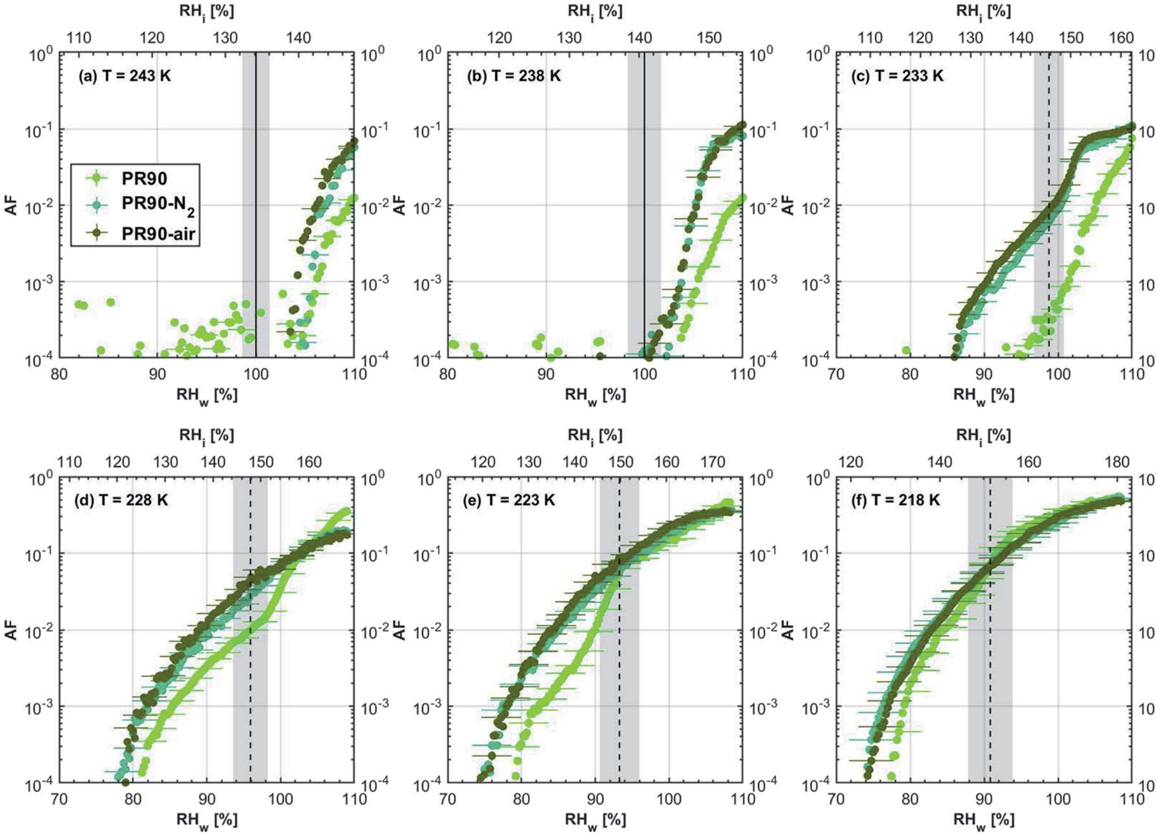

Fig. 12 The same as Fig. 9 but for fresh and denuded 400 nm PR90 soot particles.

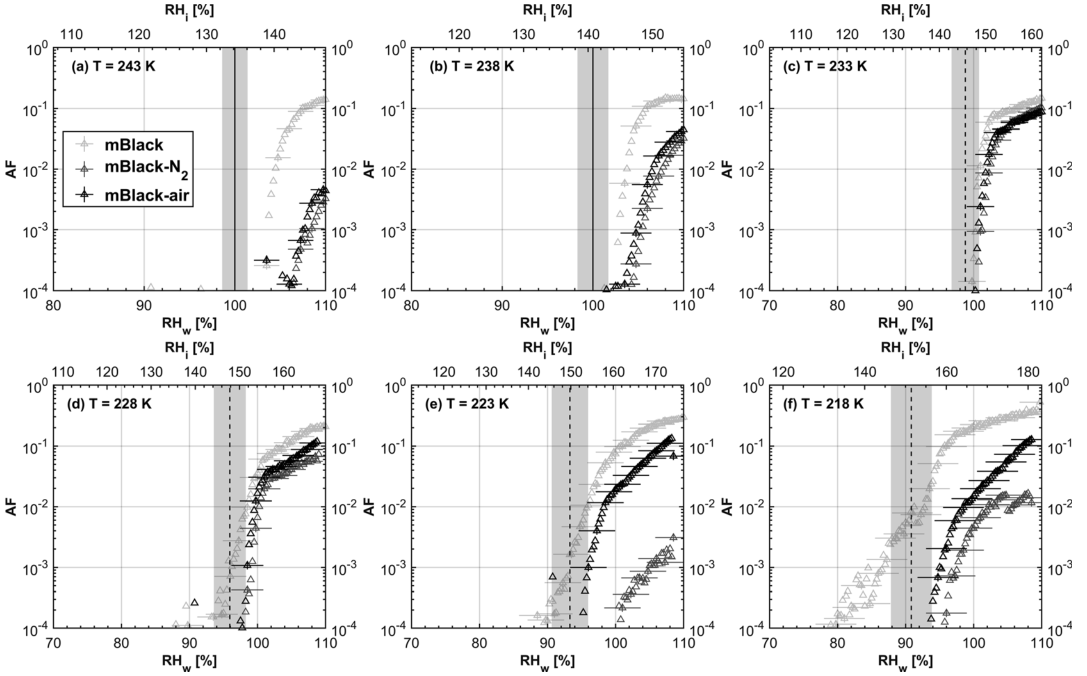

Fig. 13 The same as Fig. 9 but for fresh and denuded 200 nm mCASTblack soot particles.

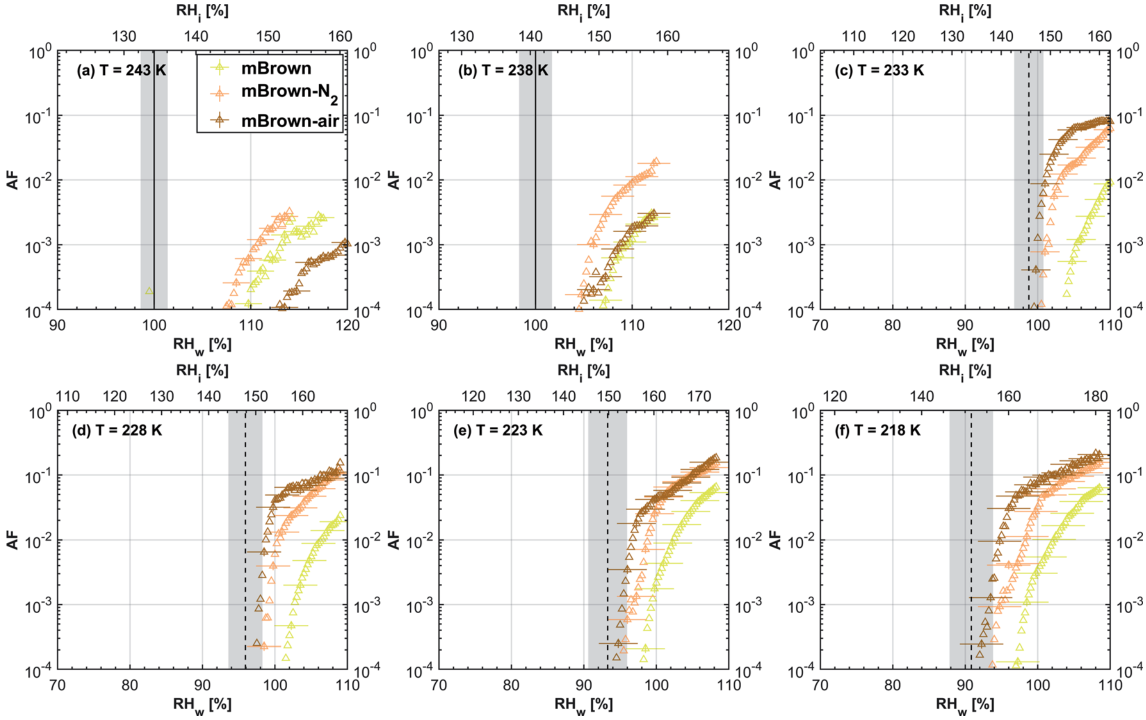

Fig. 14 The same as Fig. 9 but for fresh and denuded 200 nm mCASTbrown soot particles.

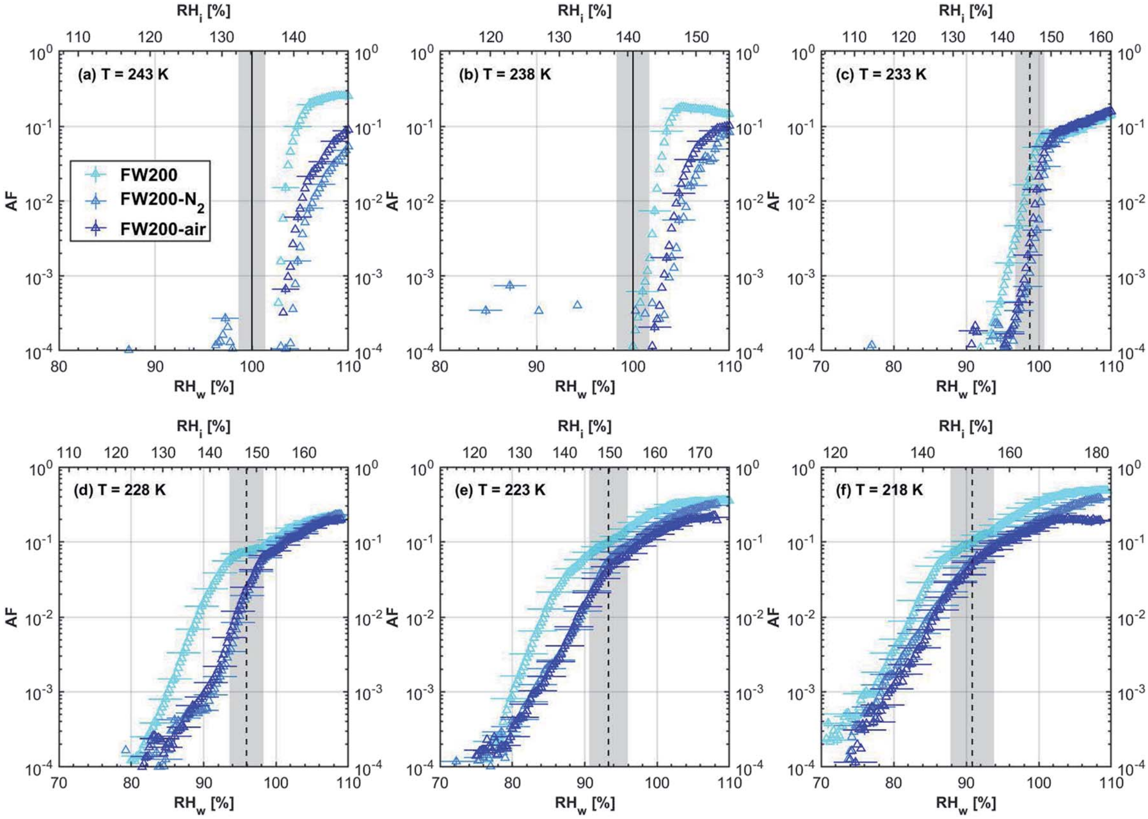

Fig. 15 The same as Fig. 9 but for fresh and denuded 200 nm FW200 soot particles.

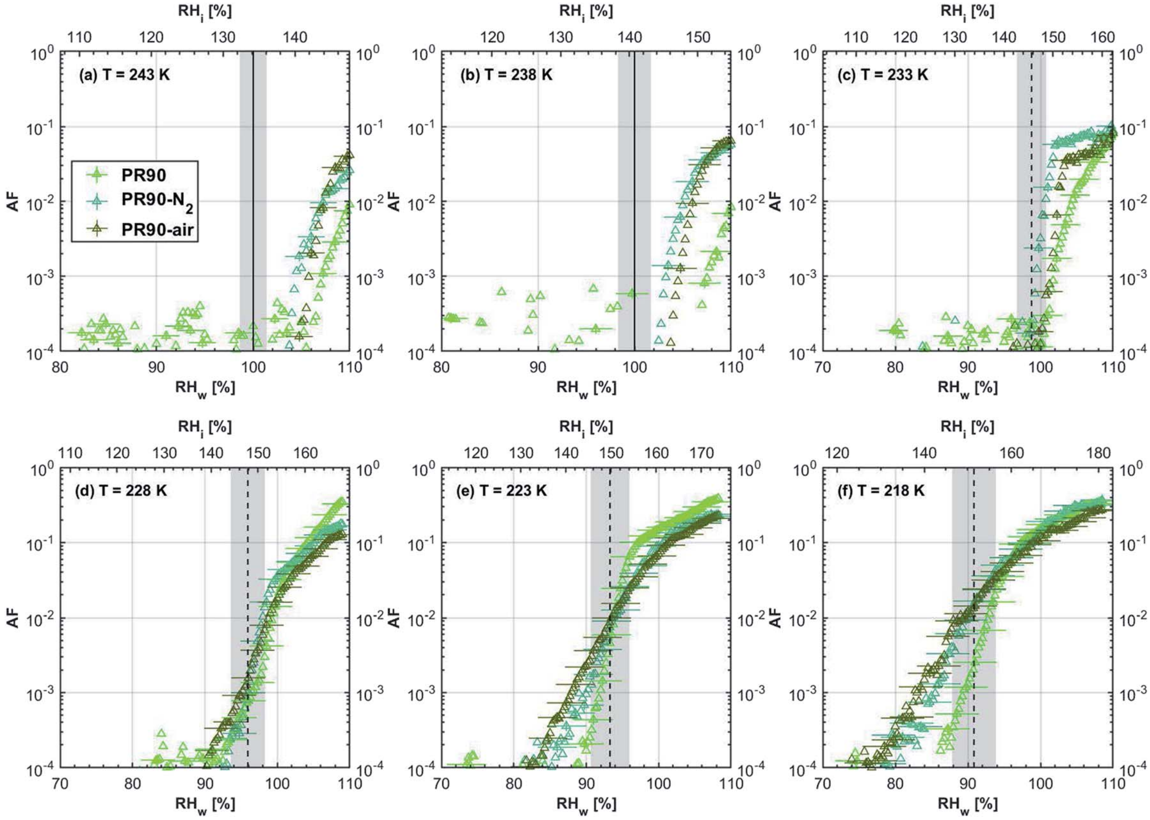

Fig. 16 The same as Fig. 9 but for fresh and denuded 200 nm PR90 soot particles.

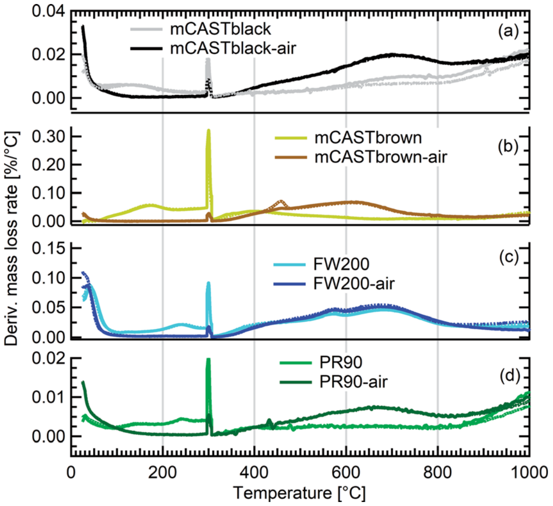

Fig. 17 TGA derivative mass loss rates as a function of temperature (*T*) for fresh and synthetic air ($N_2 + O_2$) atmosphere oven heated (300 °C) bulk soot samples solid and dotted lines indicate two individual TGA runs on the same sample type.

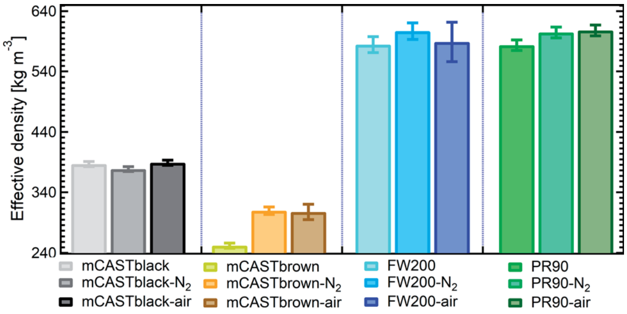

Fig. 18 The effective density (ρ_{eff}) of fresh and denuded 200 nm soot particles. The error bar indicates one standard deviation. Please note the *y*-axis origin.

particles, which suggests 200 nm FW200-N$_2$ and FW200-air particles become more densified and have decreased pore volume. This may explain the suppressed IN of both denuded 200 nm FW200 particles for *T* between 223 and 233 K (see Fig. 3c). Both denuded 200 nm PR90 particles also show a slight ρ_{eff} increase, suggesting thermal denuding induced mobility diameter reduction exceeds mass loss (see ESI S2†) because of the low volatile content of original PR90.

Author contributions

K. G. and Z. A. K. designed the experiment and interpreted the data. H. C.-K. and Z. A. K. helped K. G. with the FTIR experiment. K. G. conducted experiments and data analysis. K. G. wrote the manuscript and prepared the figures with contributions from Z. A. K. All authors discussed and reviewed the manuscript. Z. A. K. supervised the project.

Conflicts of interest

The authors declare that they have no conflict of interest.

Acknowledgements

We are grateful to the experimental atmospheric physics group at ETH Zurich for their help with instrument trouble shooting. We would like to thank Prof. Ingo Burgert (Department of Civil, Environmental and Geomatic Engineering, ETHZ) for providing access to their TGA and FTIR facilities. This work was supported by China Scholarship Council (grant no. 201906020041) and the Experimental Atmospheric Physics Professorship at ETH Zurich.

Notes and references

1 R. W. Stratton, P. J. Wolfe and J. I. Hileman, Impact of aviation non-CO(2) combustion effects on the environmental feasibility of alternative jet fuels, *Environ. Sci. Technol.*, 2011, **45**, 10736–10743.
2 T. Takemura and K. Suzuki, Weak global warming mitigation by reducing black carbon emissions, *Sci. Rep.*, 2019, **9**, 4419.
3 Z. McGraw, T. Storelvmo, B. H. Samset and C. W. Stjern, Global radiative impacts of black carbon acting as ice nucleating particles, *Geophys. Res. Lett.*, 2020, **47**, e2020GL089056.
4 U. Schumann and A. J. Heymsfield, On the life cycle of individual contrails and contrail cirrus, *Meteorol. Monogr.*, 2017, **58**, 3.1–3.24.
5 A. Bier and U. Burkhardt, Variability in Contrail Ice Nucleation and Its Dependence on Soot Number Emissions, *J. Geophys. Res.: Atmos.*, 2019, **124**, 3384–3400.
6 U. Lohmann, F. Friebel, Z. A. Kanji, F. Mahrt, A. A. Mensah and D. Neubauer, Future warming exacerbated by aged-soot effect on cloud formation, *Nat. Geosci.*, 2020, **13**, 674–680.
7 C. Alcala-Jornod, H. van den Bergh and M. J. Rossi, Can soot particles emitted by airplane exhaust contribute to the formation of aviation contrails and cirrus clouds?, *Geophys. Res. Lett.*, 2002, **29**, 1–4.
8 O. B. Popovicheva, N. M. Persiantseva, E. E. Lukhovitskaya, N. K. Shonija, N. A. Zubareva, B. Demirdjian, D. Ferry and J. Suzanne, Aircraft engine soot as contrail nuclei, *Geophys. Res. Lett.*, 2004, **31**, L11104.
9 B. Karcher, Formation and radiative forcing of contrail cirrus, *Nat. Commun.*, 2018, **9**, 1824.
10 D. S. Lee, D. W. Fahey, A. Skowron, M. R. Allen, U. Burkhardt, Q. Chen, S. J. Doherty, S. Freeman, P. M. Forster, J. Fuglestvedt, A. Gettelman, R. R. De Leon, L. L. Lim, M. T. Lund, R. J. Millar, B. Owen, J. E. Penner, G. Pitari, M. J. Prather, R. Sausen and L. J. Wilcox, The contribution of global aviation to anthropogenic climate forcing for 2000 to 2018, *Atmos. Environ.*, 2021, **244**, 117834.
11 F. Mahrt, C. Marcolli, R. O. David, P. Grönquist, M. E. J. Barthazy, U. Lohmann and Z. A. Kanji, Ice nucleation abilities of soot particles determined with the Horizontal Ice Nucleation Chamber, *Atmos. Chem. Phys.*, 2018, **18**, 13363–13392.
12 L. Nichman, M. Wolf, P. Davidovits, T. B. Onasch, Y. Zhang, D. R. Worsnop, J. Bhandari, C. Mazzoleni and D. J. Cziczo, Laboratory study of the heterogeneous ice nucleation on black-carbon-containing aerosol, *Atmos. Chem. Phys.*, 2019, **19**, 12175–12194.
13 K. Gao, C.-W. Zhou, E. J. B. Meier and Z. A. Kanji, Laboratory studies of ice nucleation onto bare and internally mixed soot–sulfuric acid particles, *Atmos. Chem. Phys.*, 2022, **22**, 5331–5364.
14 F. Mahrt, P. A. Alpert, J. Dou, P. Gronquist, P. C. Arroyo, M. Ammann, U. Lohmann and Z. A. Kanji, Aging induced changes in ice nucleation activity of combustion aerosol as determined by near edge X-ray absorption fine structure (NEXAFS) spectroscopy, *Environ. Sci.: Processes Impacts*, 2020, **22**, 895–907.
15 F. Mahrt, K. Kilchhofer, C. Marcolli, P. Grönquist, R. O. David, M. Rösch, U. Lohmann and Z. A. Kanji, The impact of cloud processing on the ice nucleation abilities of soot particles at cirrus temperatures, *J. Geophys. Res.: Atmos.*, 2020, **125**, 1–23.
16 K. Gao, F. Friebel, C.-W. Zhou and Z. A. Kanji, Enhanced soot particle ice nucleation ability induced by aggregate compaction and densification, *Atmos. Chem. Phys.*, 2022, **22**, 4985–5016.
17 M. Thommes, K. Kaneko, A. V. Neimark, J. P. Olivier, F. Rodriguez-Reinoso, J. Rouquerol and K. S. W. Sing, Physisorption of gases, with special reference to the evaluation of surface area and pore size distribution (IUPAC Technical Report), *Pure Appl. Chem.*, 2015, **87**, 1051–1069.
18 C. Marcolli, Deposition nucleation viewed as homogeneous or immersion freezing in pores and cavities, *Atmos. Chem. Phys.*, 2014, **14**, 2071–2104.
19 C. Marcolli, F. Mahrt and B. Kärcher, Soot-PCF: Pore condensation and freezing framework for soot aggregates, *Atmos. Chem. Phys.*, 2021, **21**, 7791–7843.
20 R. O. David, C. Marcolli, J. Fahrni, Y. Qiu, Y. A. Perez Sirkin, V. Molinero, F. Mahrt, D. Bruhwiler, U. Lohmann and Z. A. Kanji, Pore condensation and freezing is responsible for ice formation below water saturation for porous particles, *Proc. Natl. Acad. Sci. U. S. A.*, 2019, **116**, 8184–8189.
21 R. L. Vander Wal, V. M. Bryg and C.-H. Huang, Aircraft engine particulate matter: Macro- micro- and nanostructure by HRTEM and chemistry by XPS, *Combust. Flame*, 2014, **161**, 602–611.
22 I. Marhaba, D. Ferry, C. Laffon, T. Z. Regier, F.-X. Ouf and P. Parent, Aircraft and miniCAST soot at the nanoscale, *Combust. Flame*, 2019, **204**, 278–289.
23 A. Liati, D. Schreiber, P. A. Alpert, Y. Liao, B. T. Brem, P. Corral Arroyo, J. Hu, H. R. Jonsdottir, M. Ammann and P. Dimopoulos Eggenschwiler, Aircraft soot from conventional fuels and biofuels during ground idle and climb-out conditions: Electron microscopy and X-ray micro-spectroscopy, *Environ. Pollut.*, 2019, **247**, 658–667.

24 K. S. Johnson, B. Zuberi, L. T. Molina, M. J. Molina, M. J. Iedema, J. P. Cowin, D. J. Gaspar, C. Wang and A. Laskin, Processing of soot in an urban environment case study from the Mexico City Metropolitan Area, *Acc. Chem. Res.*, 2005, **5**, 3033–3043.

25 J. Bhandari, S. China, K. K. Chandrakar, G. Kinney, W. Cantrell, R. A. Shaw, L. R. Mazzoleni, G. Girotto, N. Sharma, K. Gorkowski, S. Gilardoni, S. Decesari, M. C. Facchini, N. Zanca, G. Pavese, F. Esposito, M. K. Dubey, A. C. Aiken, R. K. Chakrabarty, H. Moosmuller, T. B. Onasch, R. A. Zaveri, B. V. Scarnato, P. Fialho and C. Mazzoleni, Extensive soot compaction by cloud processing from laboratory and field observations, *Sci. Rep.*, 2019, **9**, 11824.

26 O. Möhler, C. Linke, H. Saathoff, M. Schnaiter, R. Wagner, A. Mangold, M. Krämer and U. Schurath, Ice nucleation on flame soot aerosol of different organic carbon content, *Meteorol. Z.*, 2005, **14**, 477–484.

27 I. Crawford, O. Möhler, M. Schnaiter, H. Saathoff, D. Liu, G. McMeeking, C. Linke, M. Flynn, K. N. Bower, P. J. Connolly, M. W. Gallagher and H. Coe, Studies of propane flame soot acting as heterogeneous ice nuclei in conjunction with single particle soot photometer measurements, *Atmos. Chem. Phys.*, 2011, **11**, 9549–9561.

28 C. Zhang, Y. Zhang, M. J. Wolf, L. Nichman, C. Shen, T. B. Onasch, L. Chen and D. J. Cziczo, The effects of morphology, mobility size, and secondary organic aerosol (SOA) material coating on the ice nucleation activity of black carbon in the cirrus regime, *Atmos. Chem. Phys.*, 2020, **20**, 13957–13984.

29 B. Friedman, G. Kulkarni, J. Beránek, A. Zelenyuk, J. A. Thornton and D. J. Cziczo, Ice nucleation and droplet formation by bare and coated soot particles, *J. Geophys. Res.*, 2011, **116**, D17203.

30 Z. A. Kanji, A. Welti, J. C. Corbin and A. A. Mensah, Black Carbon Particles Do Not Matter for Immersion Mode Ice Nucleation, *Geophys. Res. Lett.*, 2020, **46**, e2019GL086764.

31 B. Demirdjian, D. Ferry, J. Suzanne, O. B. Popovicheva, N. M. Persiantseva, A. V. Kamaev, N. K. Shonija and N. A. Zubareva, Freezing of water adsorbed on hydrophobic and activated soot particles, *Chem. Phys. Lett.*, 2009, **480**, 247–252.

32 B. Gorbunov, A. Baklanov, N. Kakutkina, H. L. Windsor and R. Toumi, Ice nucleation on soot particles, *J. Aerosol Sci.*, 2001, **32**, 199–215.

33 E. D. Kireeva, O. B. Popovicheva, N. M. Persiantseva, T. D. Khokhlova and N. K. Shonija, Effect of black carbon particles on the efficiency of water droplet freezing, *Colloid J.*, 2009, **71**, 353–359.

34 K. A. Koehler, P. J. DeMott, S. M. Kreidenweis, O. B. Popovicheva, M. D. Petters, C. M. Carrico, E. D. Kireeva, T. D. Khokhlova and N. K. Shonija, Cloud condensation nuclei and ice nucleation activity of hydrophobic and hydrophilic soot particles, *Phys. Chem. Chem. Phys.*, 2009, **11**, 7759.

35 T. Hausler, P. Gebhardt, D. Iglesias, C. Rameshan, S. Marchesan, D. Eder and H. Grothe, Ice nucleation activity of graphene and graphene oxides, *J. Phys. Chem. C*, 2018, **122**, 8182–8190.

36 L. Lupi and V. Molinero, Does hydrophilicity of carbon particles improve their ice nucleation ability?, *J. Phys. Chem. A*, 2014, **118**, 7330–7337.

37 L. Lupi, A. Hudait and V. Molinero, Heterogeneous nucleation of ice on carbon surfaces, *J. Am. Chem. Soc.*, 2014, **136**, 3156–3164.

38 T. F. Whale, M. Rosillo-Lopez, B. J. Murray and C. G. Salzmann, Ice nucleation properties of oxidized carbon nanomaterials, *J. Phys. Chem. Lett.*, 2015, **6**, 3012–3016.

39 Y. Bi, R. Cabriolu and T. Li, Heterogeneous Ice Nucleation Controlled by the Coupling of Surface Crystallinity and Surface Hydrophilicity, *J. Phys. Chem. C*, 2016, **120**, 1507–1514.

40 C. I. Biggs, C. Packer, S. Hindmarsh, M. Walker, N. R. Wilson, J. P. Rourke and M. I. Gibson, Impact of sequential surface-modification of graphene oxide on ice nucleation, *Phys. Chem. Chem. Phys.*, 2017, **19**, 21929–21932.

41 P. Cabrera-Sanfelix and G. R. Darling, Dissociative adsorption of water at vacancy defects in graphite, *J. Phys. Chem. C*, 2007, **111**, 18258–18263.

42 Z. A. Kanji and J. P. D. Abbatt, The University of Toronto Continuous Flow Diffusion Chamber (UT-CFDC): A Simple Design for Ice Nucleation Studies, *Aerosol Sci. Technol.*, 2009, **43**, 730–738.

43 L. Lacher, U. Lohmann, Y. Boose, A. Zipori, E. Herrmann, N. Bukowiecki, M. Steinbacher and Z. A. Kanji, The horizontal ice nucleation chamber (HINC): INP measurements at conditions relevant for mixed-phase clouds at the high altitude research station Jungfraujoch, *Atmos. Chem. Phys.*, 2017, **17**, 15199–15224.

44 D. M. Murphy and T. Koop, Review of the vapour pressures of ice and supercooled water for atmospheric applications, *Q. J. R. Meteorol. Soc.*, 2005, **131**, 1539–1565.

45 T. Koop, B. Luo, A. Tsias and T. Peter, Water activity as the determinant for homogeneous ice nucleation in aqueous solutions, *Nature*, 2000, **406**, 4.

46 N. M. Persiantseva, O. B. Popovicheva and N. K. Shonija, Wetting and hydration of insoluble soot particles in the upper troposphere, *J. Environ. Monit.*, 2004, **6**, 939–945.

47 O. B. Popovitcheva, N. M. Persiantseva, M. E. Trukhin, G. B. Rulev, N. K. Shonija, Y. Ya. Buriko, A. M. Starik, B. Demirdjian, D. Ferry and J. Suzanne, Experimental characterization of aircraft combustor soot: Microstructure, surface area, porosity and water adsorption, *Phys. Chem. Chem. Phys.*, 2000, **2**, 4421–4426.

48 A. Wheeler, *Reaction rates and selectivity in catalyst pores*, Reinhold publishing corp., New York, NY, 1955.

49 E. I. Shkol'nikov and E. V. Sidorova, Analytical equation for calculating the pore size distribution from adsorption data, *Dokl. Phys. Chem.*, 2007, **412**, 4–7.

50 M. M. Dubbin, Water vapor adsorption and the microporous structures of carbonaceous adsorbents, *Carbon*, 1980, **18**, 355–364.

51 J. Bhandari, S. China, T. Onasch, L. Wolff, A. Lambe, P. Davidovits, E. Cross, A. Ahern, J. Olfert, M. Dubey and C. Mazzoleni, Effect of thermodenuding on the structure of nascent flame soot aggregates, *Atmos*, 2017, **8**, 166.

52 M. N. Ess, D. Ferry, E. D. Kireeva, R. Niessner, F. X. Ouf and N. P. Ivleva, *In situ* Raman microspectroscopic analysis of soot samples with different organic carbon content: Structural changes during heating, *Carbon*, 2016, **105**, 572–585.

53 G. Vali, P. J. DeMott, O. Möhler and T. F. Whale, Technical note: A proposal for ice nucleation terminology, *Atmos. Chem. Phys.*, 2015, **15**, 10263–10270.

54 L. Ickes, A. Welti, C. Hoose and U. Lohmann, Classical nucleation theory of homogeneous freezing of water: thermodynamic and kinetic parameters, *Phys. Chem. Chem. Phys.*, 2015, **17**, 5514–5537.

55 N. H. Fletcher, *The physics of rainclouds*, Cambridge, University Press, 1962.

56 K. C. Young, *Microphysical processes in clouds*, Oxford University Press, 1993.

57 P. G. Debenedetti, *Metastable liquids: concepts and principles*, Princeton University Press, 1996.

58 A. Kiselev, F. Bachmann, P. Pedevilla, S. J. Cox, A. Michaelides, D. Gerthsen and T. Leisner, Active sites in heterogeneous ice nucleation-the example of K-rich feldspars, *Science*, 2017, **355**, 367–371.

59 O. Popovicheva, N. M. Persiantseva, N. K. Shonija, P. DeMott, K. Koehler, M. Petters, S. Kreidenweis, V. Tishkova, B. Demirdjian and J. Suzanne, Water interaction with hydrophobic and hydrophilic soot particles, *Phys. Chem. Chem. Phys.*, 2008, **10**, 2332–2344.

60 B. Zobrist, C. Marcolli, D. A. Pedernera and T. Koop, Do atmospheric aerosols form glasses?, *Atmos. Chem. Phys.*, 2008, **8**, 5221–5244.

61 T. Berkemeier, M. Shiraiwa, U. Pöschl and T. Koop, Competition between water uptake and ice nucleation by glassy organic aerosol particles, *Atmos. Chem. Phys.*, 2014, **14**, 12513–12531.

62 Y. Zhang, L. Nichman, P. Spencer, J. I. Jung, A. Lee, B. K. Heffernan, A. Gold, Z. Zhang, Y. Chen, M. R. Canagaratna, J. T. Jayne, D. R. Worsnop, T. B. Onasch, J. D. Surratt, D. Chandler, P. Davidovits and C. E. Kolb, The cooling rate- and volatility-dependent glass-forming properties of organic aerosols measured by broadband dielectric spectroscopy, *Environ. Sci. Technol.*, 2019, **53**, 12366–12378.

63 K. S. Docherty, E. W. Corse, M. Jaoui, J. H. Offenberg, T. E. Kleindienst, J. D. Krug, T. P. Riedel and M. Lewandowski, Trends in the oxidation and relative volatility of chamber-generated secondary organic aerosol, *Aerosol Sci. Technol.*, 2018, **52**, 992–1004.

64 B. Zobrist, V. Soonsin, B. P. Luo, U. K. Krieger, C. Marcolli, T. Peter and T. Koop, Ultra-slow water diffusion in aqueous sucrose glasses, *Phys. Chem. Chem. Phys.*, 2011, **13**, 3514–3526.

65 M. Shiraiwa, M. Ammann, T. Koop and U. Poschl, Gas uptake and chemical aging of semisolid organic aerosol particles, *Proc. Natl. Acad. Sci.*, 2011, **108**, 11003–11008.

66 H. C. Price, J. Mattsson, Y. Zhang, A. K. Bertram, J. F. Davies, J. W. Grayson, S. T. Martin, D. O'Sullivan, J. P. Reid, A. M. J. Rickards and B. J. Murray, Water diffusion in atmospherically relevant alpha-pinene secondary organic material, *Chem. Sci.*, 2015, **6**, 4876–4883.

67 B. J. Murray, T. W. Wilson, S. Dobbie, Z. Cui, S. M. R. K. Al-Jumur, O. Möhler, M. Schnaiter, R. Wagner, S. Benz, M. Niemand, H. Saathoff, V. Ebert, S. Wagner and B. Kärcher, Heterogeneous nucleation of ice particles on glassy aerosols under cirrus conditions, *Nat. Geosci.*, 2010, **3**, 233–237.

68 B. Zobrist, T. Koop, B. P. Luo, C. Marcolli and T. Peter, Heterogeneous ice nucleation rate coefficient of water droplets coated by a nonadecanol monolayer, *J. Phys. Chem. C*, 2007, **111**, 2149–2155.

69 B. J. Murray, S. L. Broadley, T. W. Wilson, S. J. Bull, R. H. Wills, H. K. Christenson and E. J. Murray, Kinetics of the homogeneous freezing of water, *Phys. Chem. Chem. Phys.*, 2010, **12**, 10380–10387.

70 C. Marcolli, Ice nucleation triggered by negative pressure, *Sci. Rep.*, 2017, **7**, 16634.

71 C. Marcolli, Technical note: Fundamental aspects of ice nucleation *via* pore condensation and freezing including Laplace pressure and growth into macroscopic ice, *Atmos. Chem. Phys.*, 2020, **20**, 3209–3230.

72 N. H. Fletcher, Active sites and ice crystal nucleation, *J. Atmos. Sci.*, 1969, **26**, 1266–1271.

73 Z. A. Kanji, L. A. Ladino, H. Wex, Y. Boose, M. Burkert-Kohn, D. J. Cziczo and M. Krämer, Chapter 1 Overview of ice nucleating particles, in *Meteorological Monographs*, 2017, vol. 58, ch. 1.1, pp. 1.1–1.33.

74 B. R. Stanmore, J. F. Brilhac and P. Gilot, The oxidation of soot: a review of experiments, mechanisms and models, *Carbon*, 2001, **39**, 2247–2268.

75 H. Richter and J. Howard, Formation of polycyclic aromatic hydrocarbons and their growth to soot—a review of chemical reaction pathways, *Prog. Energy Combust. Sci.*, 2000, **26**, 565–608.

76 H. A. Dandajeh, N. Ladommatos, P. Hellier and A. Eveleigh, Effects of unsaturation of C2 and C3 hydrocarbons on the formation of PAHs and on the toxicity of soot particles, *Fuel*, 2017, **194**, 306–320.

77 D. Ferry, J. Suzanne, S. Nitsche, O. B. Popovitcheva and N. K. Shonija, Water adsorption and dynamics on kerosene soot under atmospheric conditions, *J. Geophys. Res.: Atmos.*, 2002, **107**, AAC 22-21–AAC 22-10.

78 O. B. Popovicheva, N. M. Persiantseva, B. V. Kuznetsov, T. A. Rakhmanova, N. K. Shonija, J. Suzanne and D. Ferry, Microstructure and Water Adsorbability of Aircraft Combustor Soots and Kerosene Flame, *J. Phys. Chem. A*, 2003, **107**, 10046–10054.

79 R. H. Moore, L. D. Ziemba, D. Dutcher, A. J. Beyersdorf, K. Chan, S. Crumeyrolle, T. M. Raymond, K. L. Thornhill, E. L. Winstead and B. E. Anderson, Mapping the

operation of the miniature combustion aerosol standard (mini-CAST) soot generator, *Aerosol Sci. Technol.*, 2014, **48**, 467–479.

80 L. Mueller, G. Jakobi, J. Orasche, E. Karg, M. Sklorz, G. Abbaszade, B. Weggler, L. Jing, J. Schnelle-Kreis and R. Zimmermann, Online determination of polycyclic aromatic hydrocarbon formation from a flame soot generator, *Anal. Bioanal. Chem.*, 2015, **407**, 5911–5922.

81 F. Portet-Koltalo and N. Machour, *Analytical methodologies for the control of particle-phase polycyclic aromatic compounds from diesel engine exhaust*, InTech, Rijeka, 2013.

82 M. Frenklach, reaction mechanism of soot formation in flames, *Phys. Chem. Chem. Phys.*, 2002, **4**, 10.

83 C. Marchal, J.-L. Delfau, C. Vovelle, G. Moréac, C. Mounaïm-Rousselle and F. Mauss, Modelling of aromatics and soot formation from large fuel molecules, *Proc. Combust. Inst.*, 2009, **32**, 753–759.

84 J. C. Chow, J. G. Watson, L. W. A. Chen, W. P. Arnott, H. Moosmüller and K. Fung, Equivalence of elemental carbon by thermal/optical reflectance and transmittance with different temperature protocols, *Environ. Sci. Technol.*, 2004, **38**, 4414–4422.

85 R. J. Countess, Interlaboratory analyses of carbonaceous aerosol samples, *Aerosol Sci. Technol.*, 1990, **12**, 114–121.

86 O. B. Popovicheva, N. M. Persiantseva, V. Tishkova, N. K. Shonija and N. A. Zubareva, Quantification of water uptake by soot particles, *Environ. Res. Lett.*, 2008, **3**, 025009.

87 H. Bladt, J. Schmid, E. D. Kireeva, O. B. Popovicheva, N. M. Perseantseva, M. A. Timofeev, K. Heister, J. Uihlein, N. P. Ivleva and R. Niessner, Impact of Fe Content in Laboratory-Produced Soot Aerosol on its Composition, Structure, and Thermo-Chemical Properties, *Aerosol Sci. Technol.*, 2012, **46**, 1337–1348.

88 S. Takahama, R. E. Schwartz, L. M. Russell, A. M. Macdonald, S. Sharma and W. R. Leaitch, Organic functional groups in aerosol particles from burning and non-burning forest emissions at a high-elevation mountain site, *Atmos. Chem. Phys.*, 2011, **11**, 6367–6386.

89 J. Coates, Interpretation of Infrared Spectra, A Practical Approach, in *Encyclopedia of Analytical Chemistry*, John Wiley & Sons, Ltd, 2006.

90 S. P. Davis, M. C. Abrams and J. W. Brault, *Fourier transform spectrometry*, Academic Press, San Diego, 2001.

91 S. Albert, K. K. Albert and M. Quack, High resolution Fourier transform infrared spectroscopy, in *Handbook of high-resolution spectroscopy*, eds. M. Quack and F. Merkt, Wiley, Hoboken, N.J., 2011, vol. 2, pp. 965–1019.

92 M. Mermoux, Y. Chabre and A. Rousseau, FTIR and C-13 NMR study of graphite oxide, *Carbon*, 1991, **29**, 469–474.

93 D. Lin-Vien, N. B. Colthup, W. G. Fateley and J. G. Grasselli, *The handbook of infrared and raman characteristic frequencies of organic molecules*, Academic Press, San Diego, 1991.

94 V. Tucureanu, A. Matei and A. M. Avram, FTIR Spectroscopy for Carbon Family Study, *Crit. Rev. Anal. Chem.*, 2016, **46**, 502–520.

95 Z. Çiplak, N. Yildiz and A. Çalimli, Investigation of graphene/Ag nanocomposites synthesis parameters for two different synthesis methods, *Fullerenes, Nanotubes, Carbon Nanostruct.*, 2014, **23**, 361–370.

96 K. Batra, S. Nayak, S. K. Behura and O. Jani, Optimizing performance parameters of chemically-derived graphene/p-Si heterojunction solar cell, *J. Nanosci. Nanotechnol.*, 2015, **15**, 4877–4882.

97 X. B. Yan, T. Xu, S. R. Yang, H. W. Liu and Q. J. Xue, Characterization of hydrogenated diamond-like carbon films electrochemically deposited on a silicon substrate, *J. Phys. D: Appl. Phys.*, 2004, **37**, 2416–2424.

98 N. B. A. Mansor, J. P. Tessonnier, A. Rinaldi, S. Reiche and M. G. Kutty, Chemically modified multi-walled carbon nanotubes (MWCNTs) with anchored acidic groups, *Sains Malays.*, 2012, **41**, 603–609.

99 P. Dubey, D. Muthukumaran, S. Dash, R. Mukhopadhyay and S. Sarkar, Synthesis and characterization of water-soluble carbon nanotubes from mustard soot, *Pramana – J. Phys.*, 2005, **65**, 681–697.

100 V. A. Chhabra, A. Deep, R. Kaur and R. Kumar, Functionalization of graphene using carboxylation process, *Int. j. adv. sci. eng. technol.*, 2012, **4**, 13–19.

101 J. Robertson, Diamond-like amorphous carbon, *Mater. Sci. Eng., R*, 2002, **37**, 129–281.

102 L. Marcinauskas, A. Grigonis, V. Valincius and P. Valatkevicius, Surface and structural analysis of carbon coatings produced by plasma jet cvd, *Mater. Sci.*, 2007, **13**, 269–272.

103 L. Shahriary and A. A. Athawale, Graphene oxide synthesized by using modified hummers approach, *Int. J. Renew. Energy Environ. Eng.*, 2014, **2**, 58–63.

104 A. C. Obreja, D. Cristea, R. Gavrila, V. Schiopu, A. Dinescu, M. Danila and F. Comanescu, Isocyanate functionalized graphene/P3HT based nanocomposites, *Appl. Surf. Sci.*, 2013, **276**, 458–467.

105 S. Bykkam, V. K. Rao, S. C. Chakra and T. Thunugunta, Synthesis and characterization of graphene oxide and its antimicrobial activity against Klebseilla and Staphylococus, *Int. j. adv. biotechnol. res.*, 2013, **4**, 142–146.

106 O. Popovicheva, M. Kistler, E. Kireeva, N. Persiantseva, M. Timofeev, V. Kopeikin and A. Kasper-Giebl, Physicochemical characterization of smoke aerosol during large-scale wildfires: Extreme event of August 2010 in Moscow, *Atmos. Environ.*, 2014, **96**, 405–414.

107 M. Ibrahim, A. Nada and D. E. Kamal, Density functional theory and FTIR spectroscopic study of carboxyl group, *Indian J. Pure Appl. Phys.*, 2005, **43**, 911–917.

108 A. B. D. Nandiyanto, R. Oktiani and R. Ragadhita, How to read and interpret FTIR spectroscope of organic material, *Indones. J. Sci. Technol.*, 2019, **4**, 79–118.

109 D. W. Seo, W. J. Yoon, S. J. Park, M. C. Jo and J. S. Kim, The preparation of multi-walled CNT–PMMA nanocomposite, *Carbon Sci.*, 2006, **7**, 266–270.

110 P. Peets, K. Kaupmees, S. Vahur and I. Leito, Reflectance FT-IR spectroscopy as a viable option for textile fiber identification, *Heritage Sci.*, 2019, **7**, 93.

111 T. J. Johnson, J. S. Olfert, J. P. R. Symonds, M. Johnson, T. Rindlisbacher, J. J. Swanson, A. M. Boies, K. Thomson,

G. Smallwood, D. Walters, Y. Sevcenco, A. Crayford, R. Dastanpour, S. N. Rogak, L. Durdina, Y. K. Bahk, B. Brem and J. Wang, Effective density and mass-mobility exponent of aircraft turbine particulate matter, *J. Propul. Power*, 2015, **31**, 573–582.

112 G. A. Joyce, W. M. Henry and R. W. Magee, Advances in structure measurements of carbon black, *Rubber World*, 2009, **240**, 27–35.

113 Y. J. Shin, Y. Wang, H. Huang, G. Kalon, A. T. Wee, Z. Shen, C. S. Bhatia and H. Yang, Surface-energy engineering of graphene, *Langmuir*, 2010, **26**, 3798–3802.

114 Y. Wei, Q. Zhang and J. E. Thompson, The Wetting Behavior of Fresh and Aged Soot Studied through Contact Angle Measurements, *Atmos. Clim. Sci.*, 2017, **07**, 11–22.

115 H. R. Pruppacher and J. D. Klett, *Microphysics of clouds and precipitation*, Kluwer, Dordrecht, 1997.

116 U. Lohmann, F. Lüönd and F. Mahrt, *An introduction to clouds from the microscale to climate*, Cambridge University Press, 2016.

117 S. Decesari, M. C. Facchini, E. Matta, F. Lettini, M. Mircea, S. Fuzzi, E. Tagliavini and J.-P. Putaud, Chemical features and seasonal variation of fine aerosol water-soluble organic compound in the PoVally Italy, *Atmos. Environ.*, 2001, **35**, 3691–3699.

118 K. S. W. Sing, D. H. Everett, R. A. W. Haul, L. Moscou, R. A. Pierotti, J. Rouquerol and T. Siemieniewska, Reporting physisorption data for gas/solid systems with special reference to the determination of surface area and porosity, *Pure Appl. Chem.*, 1985, **57**, 603–619.

119 M. N. Ess and K. Vasilatou, Characterization of a new miniCAST with diffusion flame and premixed flame options: Generation of particles with high ec content in the size range 30 nm to 200 nm, *Aerosol Sci. Technol.*, 2018, **53**, 29–44.

120 Y. Liu, C. Liu, J. Ma, Q. Ma and H. He, Structural and hygroscopic changes of soot during heterogeneous reaction with O(3), *Phys. Chem. Chem. Phys.*, 2010, **12**, 10896–10903.

121 V. Zelenay, M. E. Monge, B. D'Anna, C. George, S. A. Styler, T. Huthwelker and M. Ammann, Increased steady state uptake of ozone on soot due to UV-vis radiation, *J. Geophys. Res.*, 2011, **116**, D1130.

122 S. D. Brooks, K. Suter and L. Olivarez, Effects of chemical aging on the ice nucleation activity of soot and polycyclic aromatic hydrocarbon aerosols, *J. Phys. Chem. A*, 2014, **118**, 10036–10047.

123 C. M. Sorensen, The mobility of fractal aggregates: A review, *Aerosol Sci. Technol.*, 2011, **45**, 765–779.